Pacific Decadal Variability and Its Hydroclimate Teleconnections in CMIP6 Models

TESS WEI-PING JACOBSON[a,b] AND RICHARD SEAGER[b]

[a] *Department of Earth and Environmental Sciences, Columbia University, New York, New York*
[b] *Lamont-Doherty Earth Observatory, Palisades, New York*

(Manuscript received 6 November 2024, in final form 4 June 2025, accepted 23 June 2025)

ABSTRACT: Natural decadal climate variability in the Pacific, such as the Pacific decadal oscillation (PDO) or the interdecadal Pacific oscillation (IPO), plays a powerful role in evolving global hydroclimate on decadal time scales. Recent generations of general circulation models (GCMs) have been found to simulate the spatial pattern of the PDO well but struggle to capture temporal variability on decadal time scales. To use GCMs to project future climate, we must understand the degree to which climate models can successfully reproduce historical PDO and IPO spatial patterns, temporal behavior, and influence on hydroclimate. We calculate PDO and IPO spatial patterns and time series using 16 models within the CMIP6 archive, all with large ($n \geq 10$) ensembles, and compare them to observations in an integrated assessment of models' ability to represent Pacific decadal variability spatiotemporally. All models underestimate decadal variability in the PDO and IPO and have a westward bias in their PDO and IPO North Pacific SST anomalies. We also evaluate hydroclimate teleconnections of the PDO and IPO in models using PDO- and IPO-associated precipitation, circulation, low-cloud, and vapor pressure deficit anomalies. We show that models' underpowered decadal variability in the Pacific is consistent with their inability to reproduce large-amplitude decadal swings in precipitation in southwestern North America and that models are virtually unable to produce a 30-yr precipitation trend in the southwest of the magnitude observed from 1982 to 2011. We emphasize the importance of model fidelity in simulating Pacific decadal variability for accurate representation of decadal-scale hydroclimate change in Pacific-teleconnected land regions.

KEYWORDS: Teleconnections; Pacific decadal oscillation; Climate models; Model evaluation/performance; Decadal variability

1. Introduction

The Pacific decadal oscillation (PDO) is a natural mode of climate variability first identified in 1997 by Mantua et al. (1997) as a pattern of sea surface temperatures (SSTs) corresponding to dramatic changes in salmon production in the North Pacific basin. Large reversals of salmon production in the North Pacific had previously been noted by fishermen in the 1920s, 1940s, and 1970s, with typically opposing salmon conditions for Alaskan versus Pacific Northwest fisheries. In particular, the reversal in the late 1970s was widely described by oceanographers, fishermen, and biologists: Nitta and Yamada (1989) and Trenberth (1990) first noted the late-1970s climate regime shift in the Pacific basin, Venrick et al. (1987) linked increases in total column chlorophyll in the central North Pacific to decadal-scale climate changes, and Ebbesmeyer et al. (1991) synthesized 40 climatological and biological variables to confirm a significant change in the overall state of the Pacific basin between 1976 and 1977. If North Pacific salmon population fluctuations were the only known impact of the Pacific decadal oscillation, it would still be a worthy subject of study; nevertheless, it was quickly shown to be linked to a pan-Pacific phenomenon with global hydroclimate impacts.

The Pacific decadal oscillation is the dominant year-round pattern of variability of SSTs in the North Pacific, typically defined as the leading empirical orthogonal function (EOF) of SSTs in the Pacific north of 20°N (Mantua et al. 1997). During a positive PDO phase, SSTs in the central and western North Pacific basins are anomalously cold, while eastern equatorial and eastern North Pacific SST anomalies are anomalously warm. This is associated with a deeper low pressure system in winter over the Aleutian Islands (the "Aleutian low") in the North Pacific. Warm SSTs are also found in the Indian Ocean and subtropical Atlantic basin. SST variability in the North Pacific is strongly related to variability in the entire Pacific basin, and although the PDO is typically defined statistically, the PDO index and pattern come about as a result of interacting physical processes across the Pacific, such as Aleutian low variability, stochastic weather forcing, gyre adjustments in the North Pacific, and El Niño–Southern Oscillation (ENSO) teleconnections (Zebiak and Cane 1987; Garreaud and Battisti 1999; Newman et al. 2016; Di Lorenzo et al. 2023). The SST fingerprint of the PDO is similar to that of ENSO; however, the equatorial SST anomalies extend further into the subtropics and the magnitude of extratropical anomalies is relatively greater. The Pacific-wide expression of Pacific decadal variability is known as the interdecadal Pacific oscillation (IPO) (Power et al. 1999), characterized by a distinct tripole pattern in the North, equatorial, and South Pacific (Henley et al. 2015). The PDO and IPO are closely related in their global spatial ($r > 0.8$) and temporal expressions as well as in their global hydroclimate teleconnections, though the PDO is calculated using North Pacific SSTs and the IPO explicitly takes

---

Supplemental information related to this paper is available at the Journals Online website: https://doi.org/10.1175/JCLI-D-24-0616.s1.

Corresponding author: Tess Wei-Ping Jacobson, tessj@ldeo.columbia.edu

DOI: 10.1175/JCLI-D-24-0616.1

into account tropical and South Pacific SSTs as well, leading to a more hemispherically symmetric spatial pattern. The South Pacific decadal contribution to the IPO pattern is referred to as the South Pacific decadal oscillation (SPDO), and despite explaining a smaller fraction of total SST variance than the PDO, the SPDO has been shown to have distinct Southern Hemisphere local drivers in the atmosphere and subsurface ocean (Lou et al. 2019; Chen and Wallace 2015).

The PDO and IPO are associated with significant signals in hydroclimate through precipitation and temperature teleconnections. A positive PDO and IPO phase corresponds with warmer than usual surface air temperatures over western North America due to the strengthened Aleutian low and anomalous warm southerly wind advection, as well as warmer surface temperatures over South America, northern East Asia, and most of Africa and Australia, though the strongest temperature anomalies are found over North America (Mantua and Hare 2002). Pacific decadal variability has also been linked to changes in global mean surface temperature—the twenty-first-century “global-warming hiatus” has been attributed in part to PDO-related cool SSTs in the Pacific (Kosaka and Xie 2013; Delworth et al. 2015; Xie and Kosaka 2017).

The negative phase of the PDO is associated with decadal-scale droughts in western and central North America (Nigam et al. 1999; Dai 2013b, 2021; Seager and Ting 2017). The recent shift in southwestern North America from wetter and colder conditions in the 1980s to drier and warmer conditions in the 2000s is primarily a result of the shift from the positive phase to the negative phase of the PDO inducing a reduction in precipitation (Seager and Hoerling 2014; Delworth et al. 2015; Seager and Ting 2017; Zhao et al. 2017; Lehner et al. 2017; Seager et al. 2022b, 2023). Anthropogenic warming induces changes in the hydrological cycle in the southwestern United States that could amplify the impacts of the decadal shift in the Pacific, such as increased evaporative demand due to warming and reduced snowpack (Dai 2013a; Diffenbaugh et al. 2015; Shukla et al. 2015;Williams et al. 2015b), but these effects are for now secondary to the decadal swings in precipitation associated with the PDO in modulating the precipitation–evaporation–runoff balance (Seager et al. 2023).

Pacific decadal variability also impacts hydroclimate outside of southwestern North America. The positive phase of the PDO is associated with reduced precipitation in northern South America, sub-Saharan Africa, eastern Australia, India, and coastal East Asia (Mantua and Hare 2002). During the positive phase of the PDO, the Indian and African monsoons are weakened (Yoon and Yeh 2010; Meehl and Hu 2006; Vishnu et al. 2018; Lüdecke et al. 2021). During the negative phase of the PDO, the summer monsoon in eastern China is weakened (Zhu et al. 2015; Yang et al. 2017). In addition, decadal variability of tropical cyclone activity in the Pacific and Atlantic basins has been linked to the PDO, with more tropical cyclones making landfall in East Asia during the negative phase of the PDO (Lee et al. 2012; Wang et al. 2015; Yang et al. 2018; Lee et al. 2021; Wang and Toumi 2021; Wang et al. 2023).

Recent generations of general circulation models (GCMs) reproduce the observed spatial pattern of the PDO but struggle to capture its temporal variability and multidecadal swings. Wei et al. (2018) found that Coupled Model Intercomparison Project phase 5 (CMIP5) models accurately simulate the PDO–precipitation teleconnection in North America but are not able to correctly simulate the PDO’s impact on the western North Pacific subtropical high. Most CMIP3 and CMIP5 models are able to reproduce the PDO-like leading mode of North Pacific sea surface temperature variability but underestimate the temporal variability of the PDO (Wang and Miao 2018; Fleming and Anchukaitis 2016; Farneti 2017). CMIP6 models have been shown to reproduce the spatial pattern of the PDO to a high degree but underestimate the temporal variability of the PDO at all time scales (Coburn and Pryor 2021; Ma et al. 2023).

Future changes in Pacific decadal variability will play a large role in the evolution of global climate on decadal time scales. Therefore, to use GCMs to project future climate, we need to assess how successfully climate models reproduce historical spatial patterns and temporal behavior of Pacific decadal variability and its influence on hydroclimate. Properly simulating decadal variability is also important for explaining and attributing past changes to anthropogenic climate change (Hegerl and Zwiers 2011). Improving decadal prediction in climate models is a target of ongoing research, particularly in the Pacific (Cassou et al. 2018). Here, we examine and calculate PDO and IPO spatial patterns and principal component (PC) time series using the historical runs of sixteen models within the Coupled Model Intercomparison Project phase 6 (CMIP6) archive, chosen as those with large ($n \geq 10$) ensembles. We choose to present both model PDOs and IPOs to comprehensively evaluate both North Pacific and pan-Pacific variability in these models. Many existing studies assessing the representation of modes of climate variability in models use a single realization from each model to represent that model, yet the spread in fidelity between different realizations is often just as large or larger than the spread between different models (Coburn and Pryor 2021). To the best of our knowledge, this study comprises the most comprehensive assessment to date of the spatiotemporal features of Pacific decadal variability in a broad range of large-ensemble models within the current generation (CMIP6) and their hydroclimate teleconnections, including global teleconnections to precipitation, vapor pressure deficit (VPD), circulation, and low clouds. Section 2 introduces the CMIP6 models and observational products used in this study as well as our methods of analysis and preprocessing. In section 3, we present the spatial and temporal characteristics of model PDOs and IPOs and compare them to observed. In section 4, we evaluate model teleconnections between Pacific decadal variability and global hydroclimate anomalies, and in section 5, we show that temporal biases in modeled PDOs and IPOs are accompanied by temporal biases in models’ southwestern North America precipitation variability. In section 6, we discuss the possible mechanisms behind, and implications of, model uncertainty in Pacific decadal variability and present our conclusions.

2. Data and methodology

The 16 models from the CMIP6 archive used in this study are shown in Table 1. We choose these models based on their

TABLE 1. CMIP6 models used in this study, their associated institutions (abbreviated), ensemble size of SST data, nominal ocean resolutions, and relevant references.

	Institution	Ensemble size (n)	Ocean resolution	Reference
ACCESS-ESM1-5	CSIRO	30	1° × 1°	Ziehn et al. (2019)
CESM2	NCAR	11	1° × 1°	Danabasoglu (2019)
CNRM-CM6-1	CNRM-CERFACS	30	1° × 1°	Voldoire (2018)
CNRM-ESM2-1	CNRM-CERFACS	11	1° × 1°	Seferian (2018)
CanESM5	CCCma	65	1° × 1°	Swart et al. (2019)
EC-Earth3	EC-Earth Consortium	23	1° × 1°	EC-Earth (2019)
GISS-E2-1-G	NASA-GISS	46	1.25° × 1°	NASA/GISS (2018)
GISS-E2-1-H	NASA-GISS	25	1° × 1°	NASA/GISS (2019)
INM-CM5-0	INM	10	0.5° × 0.25°	Volodin et al. (2019)
IPSL-CM6A-LR	IPSL	32	1° × 1°	Boucher et al. (2018)
MIROC-ES2L	MIROC	31	1° × 1°	Hajima et al. (2019)
MIROC6	MIROC	50	1° × 1°	Tatebe and Watanabe (2018)
MPI-ESM1-2-HR	MPI-M	10	0.4° × 0.4°	Jungclaus et al. (2019)
MPI-ESM1-2-LR	MPI-M	10	1.5° × 1.5°	Wieners et al. (2019)
NorCPM1	NCC	21	1° × 1°	Bethke et al. (2019)
UKESM1-0-LL	MOHC	17	1° × 1°	Tang et al. (2019)

ensemble size ($n \geq 10$) of readily available ensemble members in the historical runs, for a grand ensemble size of $n = 422$ runs with SST data. In calculating CMIP6 PDOs, we focus on the 1870–2014 period to compare to observations. SST fields from each model and ensemble run are first regridded to a common 1° latitude × 1° longitude grid.

For SST observations, we use the NOAA Extended Reconstructed SST version 5 (ERSSTv5) (Huang et al. 2017) and the Met Office Hadley Centre Sea Ice and SST dataset (HadISST) version 1.1 (Rayner et al. 2003) monthly average SSTs. We present these two SST observations because both are commonly used but may have systemic differences in their North Pacific SST records that may affect their representation of the PDO (Wen et al. 2014). For observations of precipitation over land from 1901 to 2014, we use monthly mean precipitation from the Climatic Research Unit Time Series, version 4 (CRU TS) (Harris et al. 2020), and for satellite observations of precipitation, we use monthly means from the Global Precipitation Climatology Project (GPCP) dataset version 2.3 (Adler et al. 2018). Observed total cloud cover is taken from the International Satellite Cloud Climatology Project (ISCCP) data (Schiffer and Rossow 1983) bias corrected for temporal artifacts (Norris and Evan 2015) and monthly means for 1984–2009. Observed low-cloud cover is then estimated using monthly subsidence at 700 hPa (ω_{700}) from the European Centre for Medium-Range Weather Forecasts (ECMWF) ERA5 reanalysis product (Hersbach et al. 2020) to mask ISCCP data to only subsidence regions where $\omega_{700} > 0$. Low-cloud cover in CMIP6 is calculated using the total cloud data and similarly masking out regions where climatological ω_{700} is negative in the model (Figs. S12 and S13 in the online supplemental material). For geopotential height at 300 hPa, we use monthly data from version 3 of the Twentieth Century Reanalysis (20CR) (Compo et al. 2011), and for sea level pressure, we use the Hadley Centre Sea Level Pressure dataset version 2 (HadSLP2) (Allan and Ansell 2006). Vapor pressure deficit is calculated using monthly mean temperature and vapor pressure from 20CR and ERA5, as the difference between surface saturation vapor pressure (a function of temperature) and vapor pressure as in Seager et al. (2015). In CMIP6 models, VPD is calculated from the monthly mean surface air temperature and surface relative humidity. Observed net downward heat flux at the surface is calculated from monthly means of surface shortwave, longwave, and turbulent fluxes from ERA5. In calculating teleconnections, some model realizations available for SSTs were not available for certain variables, leading to ensemble sizes of $n = 419$ for precipitation and VPD, $n = 420$ for sea level pressure, $n = 399$ for geopotential height at 300 hPa, $n = 407$ for low-cloud cover, and $n = 332$ for downward heat flux at the surface.

To calculate the PDO spatial patterns and time series, we use EOF analysis. First, SST anomalies from 1870 to 2014 in the North Pacific are calculated as departures from both the global mean SST and the monthly climatology between 20° and 70°N and 100°E–110°W. Then, EOFs and PC time series are calculated (for CMIP6 models, on each run) using the xeofs Python package (Rieger and Levang 2024). The first EOF and PC time series are selected, and the PC time series is standardized. The global SST anomaly is regressed onto the standardized PC1 to make global maps of the PDO SST anomaly (SSTA) fingerprint. In calculating the IPO spatial patterns and time series in observations and models, we calculate the tripole index (TPI) for the IPO as described in Henley et al. (2015), as the 13-yr low-pass Chebyshev filtered difference between central equatorial Pacific (10°S–10°N, 170°E–90°W) SSTAs and the average of the SSTAs in the northwest (25°–45°N, 140°E–145°W) and southwest (50°–15°S, 150°E–160°W) Pacific. Due to edge effects of the 13-yr low-pass filter applied in the calculation of the TPI, the IPO time series is calculated from 1877 to 2008. PDO SSTA regression maps calculated using the 13-yr low-pass-filtered PDO are available in the supplemental material (Fig. S1). Periodograms in section 3b and the appendix are calculated using the Lomb–Scargle method due to the smooth decadal-to-interannual signal produced, though our core findings do not differ using Fourier transforms to calculate power spectra.

In section 3d, we calculate three metrics to quantify model performance in simulating spatiotemporal features of the PDO and IPO. The relative magnitude of PDO and IPO signals in the tropical versus extratropical Pacific is calculated as the ratio of the root-mean-square (RMS) magnitude of SSTAs in the equatorial Pacific (100°E–60°W and 5°S–5°N) to the RMS of SSTAs in the North Pacific (100°E–110°W and 35°–45°N). The index representing model accuracy is then calculated as the ratio of this ratio in models to this ratio in observations (ERSSTv5). Thus, a score closer to 1 would represent models having a close match to the observed tropical–extratropical signal ratio, a score greater than 1 would indicate that models overrepresent tropical variability compared to North Pacific variability, and a score less than 1 indicates that models underrepresent tropical variability compared to North Pacific variability. For the IPO, this metric is calculated as the ratio of the RMS of SSTAs in the North (25°–45°N, 140°E–145°W) and South (50°–15°S, 150°E–160°W) Pacific to the equatorial Pacific (10°S–10°N, 170°E–90°W) regions of the TPI. To correct the pattern correlation score of models (shown in Fig. 1) for accuracy in representing the magnitude of the PDO/IPO pattern, we implement a correction factor to the pattern correlation r based on the RMS SSTA in the entire Pacific basin (100°E–60°W):

$$r' = \begin{cases} r \times \exp\left(-\dfrac{|\mathrm{RMS}_{\mathrm{obs}} - \mathrm{RMS}_{\mathrm{model}}|}{\mathrm{RMS}_{\mathrm{obs}}}\right), & \text{if } \mathrm{RMS}_{\mathrm{model}} \geq \mathrm{RMS}_{\mathrm{obs}} \\ r \times \exp\left(-\dfrac{|\mathrm{RMS}_{\mathrm{obs}} - \mathrm{RMS}_{\mathrm{model}}|}{\mathrm{RMS}_{\mathrm{model}}}\right), & \text{if } \mathrm{RMS}_{\mathrm{model}} < \mathrm{RMS}_{\mathrm{obs}} \end{cases}, \tag{1}$$

where r' is the corrected pattern correlation, r is the area-weighted global pattern correlation between the observed pattern and the ensemble-mean model pattern, $\mathrm{RMS}_{\mathrm{obs}}$ is the RMS SSTA in the Pacific in the observed PDO/IPO pattern, and $\mathrm{RMS}_{\mathrm{model}}$ is the RMS SSTA in the Pacific in the model's ensemble-mean PDO/IPO pattern. In this way, a given model's pattern correlation is reduced by the correction factor if the overall magnitude of the pattern is too large or too small (see Fig. S2). Finally, the ability of a given model to represent observed temporal variability of the PDO/IPO in the decadal band (20–50 years) is quantified by the percentile of the observed power density within that model ensemble's distribution of decadal-band-averaged power densities. For the IPO, power spectra are calculated on the unfiltered TPI time series (Fig. S7).

3. Spatiotemporal evaluation of model PDOs and IPOs

a. *Spatial features of the PDO*

Here, we assess the ability of CMIP6 models to recreate the spatial features of the PDO and IPO as compared to observations. ERSSTv5 and HadISST PDO spatial patterns are highly correlated ($r = 0.96$, uncentered pattern correlation). In the positive phase of the observed PDO, a characteristic cold anomaly maximizes in the central/eastern North Pacific of around 0.7 K (per standard deviation of the PC time series) which expands westward to Japan and the basin edge (Fig. 1). This North Pacific cold anomaly is flanked to the east by a c-shaped warm anomaly along the west coast of North America. In the equatorial Pacific, the classic positive PDO pattern has a warm anomaly in the central–eastern equatorial Pacific to the west coast of South America, flanked to the west by a weak cold anomaly in the far western equatorial Pacific (Power et al. 2021; Capotondi et al. 2023). The observed PDOs have a cold anomaly in the western and central South Pacific, relatively weak compared to that in the North Pacific.

Most model PDOs spatially correlate highly ($r > 0.8$ globally) with observed PDOs and are able to capture both a cold anomaly in the western North Pacific and a warm anomaly in the eastern/central equatorial Pacific with varying degrees of similarity to the observations (Fig. 1). Model PDOs are a statistical mode of variability calculated using EOF analysis and resulting from different dynamical processes, which may differ across models. Still, model PDO time series correlate significantly with North Pacific SST anomaly time series for all models (Fig. S3), indicating that these PDO indices are indeed representative of physical changes in SST in the North Pacific. The South Pacific cool anomaly is less consistently present in model PDOs. INM-CM5-0 is the only model that fails to produce an equatorial signal in its PDO pattern. Many of the model PDOs disagree with observations on the location of the maxima in the North Pacific and equatorial Pacific, with models showing a preference for the North Pacific cool anomaly to maximize just off the coast of Japan in the Kuroshio–Oyashio extension (KOE) region rather than in the eastern-central basin. CESM2 has the strongest pattern correlation with observations ($r = 0.91$ with ERSSTv5 and $r = 0.90$ with HadISST), yet in the North Pacific the ensemble-mean PDO pattern has maximum cooling in the KOE region with a secondary maximum in the eastern-central basin.

We use three metrics to quantitatively assess the accuracy of models in recreating the spatial pattern of the PDO: the longitudes of the North Pacific and equatorial Pacific extrema, the SST gradients across the North Pacific and equatorial Pacific, and the latitudinally weighted RMS SST anomaly (SSTA) in the North Pacific and the equatorial Pacific (Fig. 2). While almost every model PDO captures a cool anomaly in the North Pacific and a warm anomaly in the equatorial Pacific, there is a broad range of longitudes over which these features maximize among the models and their individual ensemble members. PDOs calculated from ERSST and HadISST have North Pacific cool anomalies that are strongest around 160°, far on the eastward tail of the distribution for the grand ensemble of CMIP6 models examined. The ERSST longitude is in the 99th percentile, and the HadISST longitude is further east than any ensemble members. The 25% of model realizations have maximum cool extrema at 144.5°E off the coast of Japan. All models except for MIROC6 and MIROC-ES2L have their ensemble-mean North Pacific extrema between 140° and 150°E. Some models, namely, CESM2, CNRM-CM6-1, MIROC6, MIROC-ES2L, and NorCPM1, have secondary maxima in the central/eastern North Pacific despite their largest cool anomalies

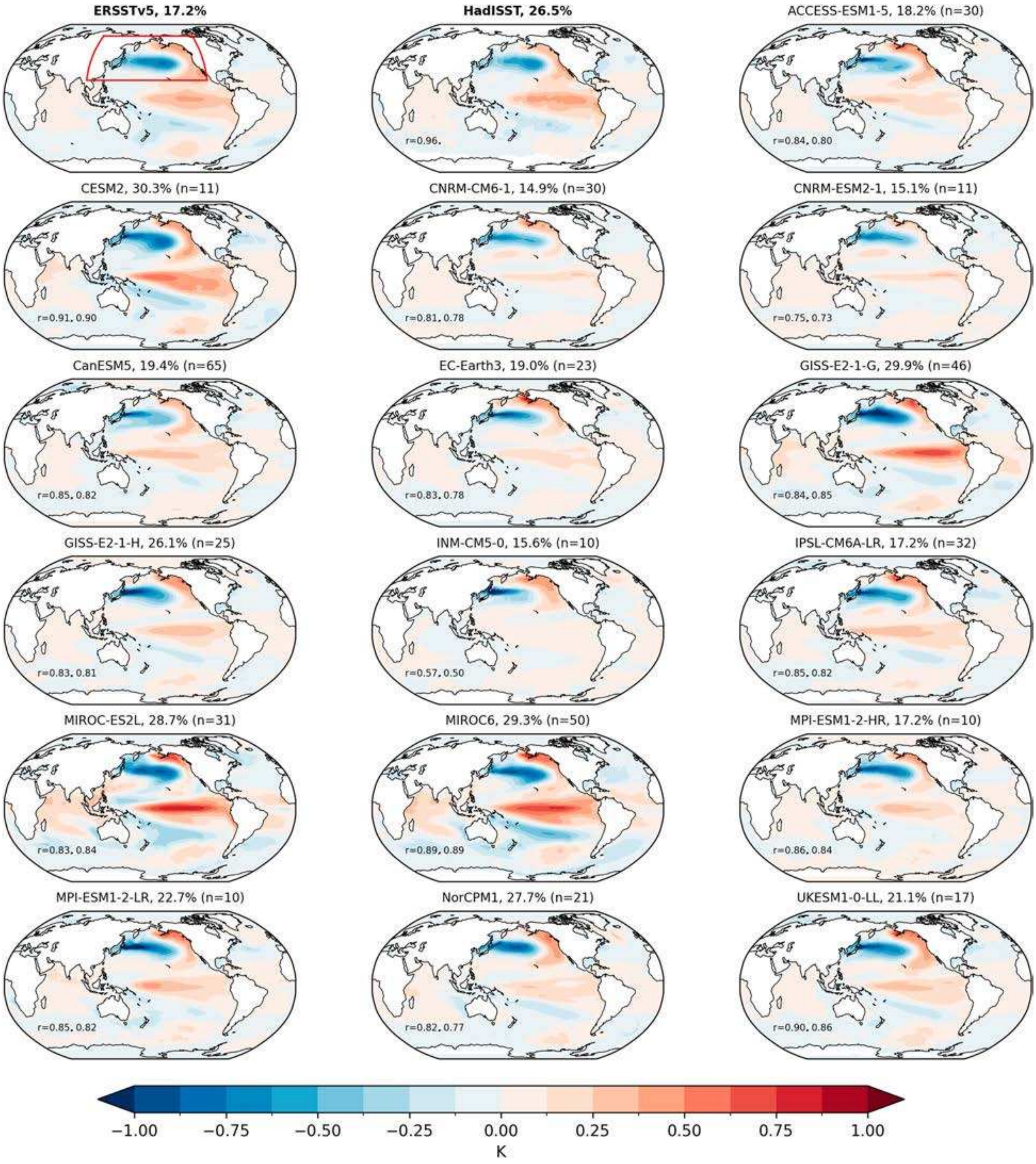

FIG. 1. Global SSTA regressed onto PDO time series for observations and models with multiple ensemble members and explained variance of the PDO PC1 time series. Model SSTA patterns and explained variances are calculated as the overall means of *n* ensemble member's PDO SSTA patterns. Bottom-left corner of each panel shows the area-weighted pattern correlation with ERSSTv5 and HadISST, respectively. Red box outlines the region over which the EOF is calculated.

occurring in the KOE region (Fig. 1). The observed PDO maxima in the equatorial region sit more within the model range of longitudes; model PDOs have a bimodal distribution of equatorial extrema, with most models peaking between 160°E and 180° and another group of models peaking east of 140°W. The two observed PDOs differ slightly in this metric as well, with the ERSSTv5 warm maximum around 138°W and the HadISST warm maximum around 112°W, both further east of where most of the models and ensemble members tend to have their equatorial maxima.

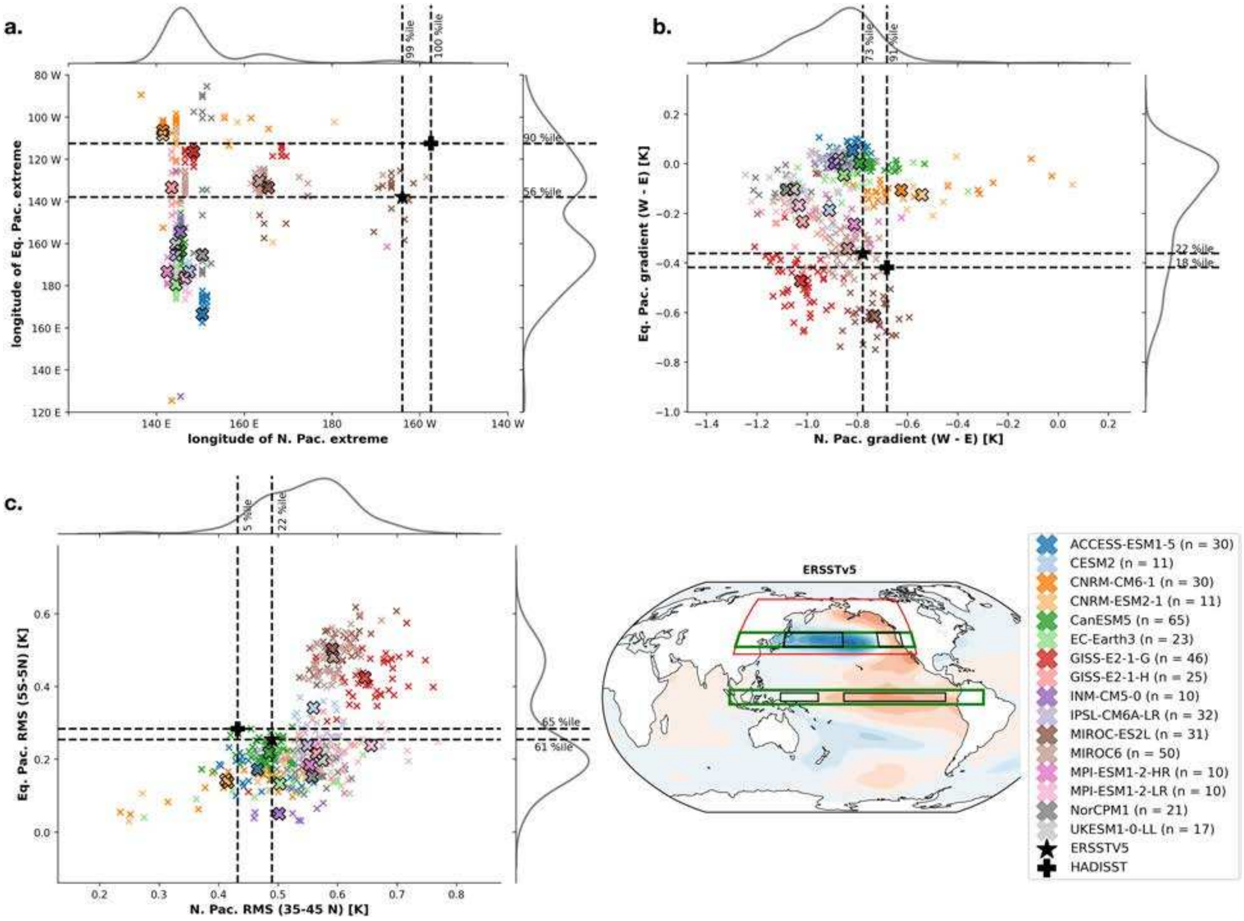

FIG. 2. (a) Longitudes of the maximum magnitude of SSTA within the equatorial Pacific (5°S–5°N; *y* axis; green tropical box in lower right) and North Pacific (30°–70°N; *x* axis; red box in lower right) of PDO SSTA patterns for each model ensemble and for ERSSTv5 (black star) and HadISST observations (black cross). (b) West-to-east gradient across the equatorial (*y* axis) and North (*x* axis) Pacific. The equatorial Pacific gradient is calculated as the difference between the SST in a western box (140°–170°E, 3°S–3°N) and an eastern box (170°–90°W, 3°S–3°N), and the North Pacific gradient is calculated as the difference between the average SST in a western box (140°E–170°W, 35°–45°N) and an eastern box (140°–120°W, 35°–45°N). These boxes are outlined in black in the lower-right panel. (c) The RMS magnitude in the equatorial Pacific (100°E–60°W and 5°S–5°N; *y* axis) and North Pacific (100°E–110°W and 35°–45°N; *x* axis). These boxes are outlined in green in the lower-right panel. Small colored markers show individual ensemble members, while bold colored markers show the values for the ensemble-mean pattern. Margins show the kernel density estimates (KDEs) of the distribution of the grand ensemble, and lines and percentile markings indicate the percentiles of the observations within the grand ensemble mean. (bottom right) The ERSSTv5 PDO pattern from Fig. 1 with key regions outlined.

The longitudinal gradients of the PDO patterns in the North and equatorial Pacific are shown in the top-right panel of Fig. 2. The North Pacific gradient is calculated as the difference between the average SST in a western box (140°E–170°W, 35°–45°N) and an eastern box (180°W–160°, 35°–45°N), with these boxes selected to best capture the observed North Pacific gradient in the PDO. Similarly, the equatorial Pacific gradient is calculated as the difference between the SST in a western box (140°–170°E, 3°S–3°N) and an eastern box (170°–90°W, 3°S–3°N), as in Seager et al. (2022a). The observed PDO patterns have North Pacific gradients of ≈−0.7 and −0.8 K. Most model ensemble members have too negative a gradient, with too large of a cool anomaly, too weak of a warm anomaly, or both. This is consistent with all models having a cool anomaly that is too far west compared with observations; in the observed PDO, the SST becomes less negative westward from the date line in the North Pacific, while in most models, it decreases to a cold extreme near Japan (Fig. 1). In the equatorial Pacific, the observed PDO patterns have gradients of ≈−0.4 K and are in the 18th and 22nd percentiles of the model distribution. This bias is likely related to the well-documented excessive westward extension in ENSO SST patterns in CMIP models of multiple generations (Gong et al. 2015; Jiang et al. 2021; Capotondi et al. 2020). Most models have a negative equatorial PDO gradient that is too weak, due to their warm anomalies being too weak, too far west, or both. The ACCESS model has the wrong sign equatorial gradient, and the IPSL, INM, and CanESM models have nearly no equatorial gradient.

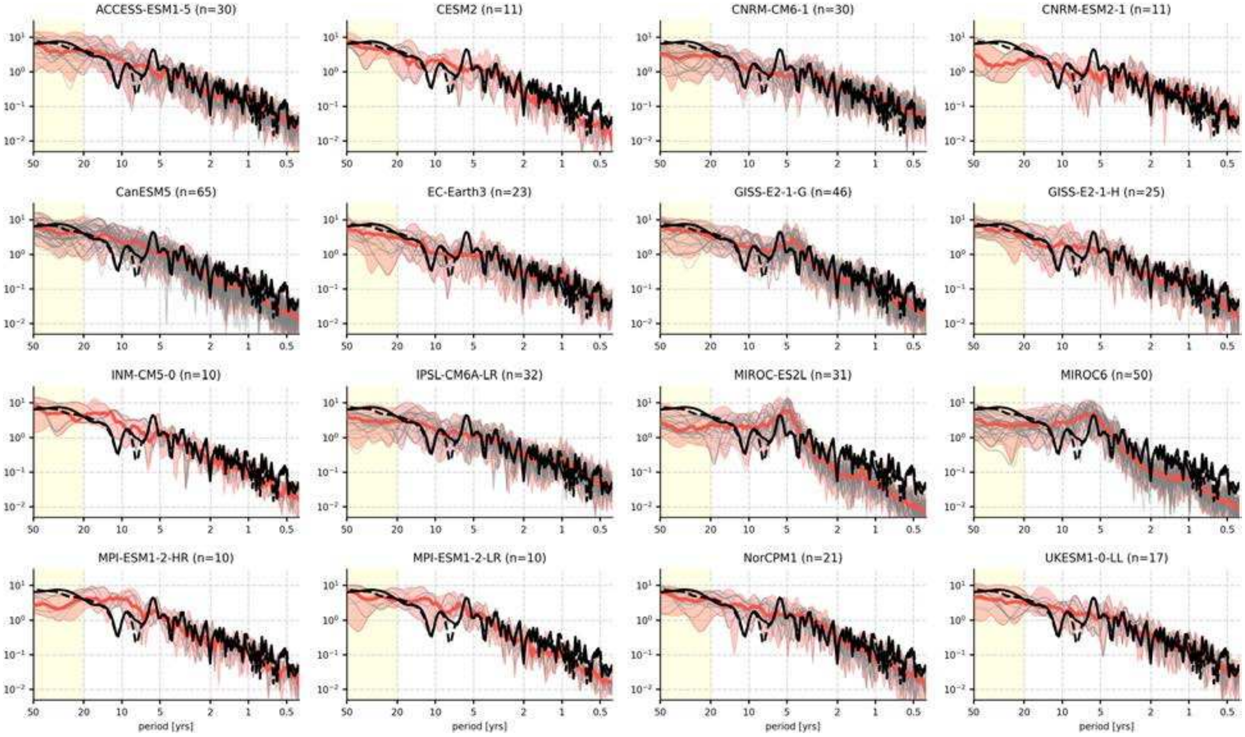

FIG. 3. Power spectral density by periods for PDO time series from 1870 to 2014 from model runs (thin gray lines) vs observations (ERSSTv5; thick black solid line; HadISST, thick black dotted line). Ensemble means are shown by the thick red line, and red envelopes show 95% confidence intervals. Yellow highlighted region represents the decadal band of periods between 20 and 50 years.

Finally, the RMS SSTAs in the North Pacific and equatorial Pacific give a measure of the magnitude of the spatial variability in these regions. For our purposes, the North Pacific region is defined as 100°E–120°W and 35°–45°N, and the equatorial Pacific region is defined as 100°E–120°W and 5°S–5°N. The observed PDOs have RMS in the North Pacific of between 0.4 and 0.5 K (5th and 22nd percentiles of the model distribution) and RMS in the equatorial Pacific between 0.25 and 0.3 K (61st and 65th percentiles of the model distribution). Most models have too weak spatial variance in the equatorial Pacific and too strong spatial variance in the North Pacific. The exceptions in this regard are MIROC6, MIROC-ES2L, GISS-E2-1-G, and CESM2, which have stronger spatial variance in both the North Pacific and the equatorial Pacific. Notably, these four models do particularly well at correctly simulating the location of the cold anomaly in the North Pacific with a secondary maximum or eastward extension that is near the longitude of the cold maximum in observations (Fig. 1). The result from the four models suggests that the overestimate of the tropical anomalies may be associated with an overestimate of the anomalies in the North Pacific. In addition, there is a large spread in the values shown in Figs. 2b and 2c for realizations within a given model, particularly for the CNRM models. Certain models have a range in fidelity in reproducing the observed PDO pattern both in the Pacific and globally that is broader than the range of model ensemble means (Figs. S4 and S5), indicating that, for those models, intramodel spread may play an important role in model PDO simulation uncertainty.

b. *Temporal features of the PDO*

Periodograms in Fig. 3 show the power density of model PDO time series for different periods compared to the observed (ERSSTv5) PDO periodogram (black line). The characteristic PDO power spectrum has two peaks that rise above 95% significance according to a first-order autoregressive [AR(1)] model (not shown): one in the decadal band, between 20 and 50 years, and one in the ENSO band, between 5 and 7 years. With the relatively short observational record of SSTs, it is difficult to evaluate the preferred frequencies of variability of the PDO index. However, there is a general consensus that spectral power increases from periods of about 10 years to periods of 50 years or greater (Newman et al. 2016; Zhang et al. 2018; Oshima and Tanimoto 2009). Most model periodograms show decreasing power in periods shorter than 50 years, but also underestimate the PDO power in the 20–50-yr band, consistent with similar findings from previous generations of models (Farneti 2017). While the two observed power spectra sit within or slightly above the model envelope in the 20–50-yr band for most models, this underestimation is persistent for all models and the band-averaged observed power is above the 70th percentile of models for every model (see section 3d). Additionally, a few models (GISS-E2-G, MIROC6, and MIROC-E2SL) have large peaks in the ENSO band, with more power in ENSO frequencies than in PDO frequencies. In the Niño-3.4 region, these models also have too much temporal variability in ENSO frequencies and too little decadal variability (Fig. S6).

c. *Interdecadal Pacific oscillation*

Here, we examine the TPI of the IPO in models and observations (Henley et al. 2015).

Observed PDO and IPO global SST patterns correlate with each other with $r > 0.8$ (not shown), demonstrating the close relationship between PDO and IPO SSTs despite the explicit inclusion of equatorial and South Pacific SSTs in the calculation of the IPO. Both include in their positive phase a cool western North Pacific and warm eastern and central equatorial Pacific, with warm SSTs along the coast of North America and a local maximum off Baja California. The observed IPO, however, is more symmetric about the equator, with more prominent cool SSTs in the western South Pacific and warm SSTs off the coast of Chile and in the Southern Ocean north of West Antarctica (Fig. 4). In general, model pattern correlations with observations for the IPO pattern are lower than those for the PDO pattern. Some models with undersized or no expression of the PDO in the tropical and South Pacific (such as INM-CM5-0) appear to have more IPO variability in these regions. Similar to the PDO, we find that most models have a bias such that maximum cooling occurs in the KOE region, while the observed cooling maximum is in the central North Pacific. Most models have too much variability in the North and equatorial Pacific. In addition, all models struggle to capture the observed degree of variability in the South Pacific region, and several models (e.g., CESM2) are asymmetric about the equator in the tropical Pacific, with larger anomalies in the southeastern equatorial Pacific. Outside of the Pacific, the CNRM models have too large of a cooling in the North Atlantic, while CanESM5 shows warming in the North Atlantic contrary to observations. The overall model biases in spatial patterns for the IPO are similar to those of the PDO: a westward shift in the North Pacific cool maxima and a too zonally broad equatorial warming. Due to the outsized signal of the IPO in the North and equatorial Pacific compared to the South Pacific, we present the relative strength of the IPO pattern in each of the North, South, and equatorial Pacific regions in Fig. 5. The two observational products generally agree on the average magnitudes in the North, South, and equatorial Pacific. The overall discrepancy of models from observations is clear: Models have too weak an IPO signal in the South Pacific and too strong a signal in the tropics. In observations, the South Pacific signal is slightly weaker than that of the North Pacific, but models have systematically too weak South Pacific SST anomalies associated with the IPO. CanESM5 stands out with too weak a signal in the North Pacific, too strong a signal in the equatorial Pacific, and the wrong sign signal in the South Pacific in the ensemble mean. While CanESM5 correctly simulates the observed ratio of the equatorial Pacific to North Pacific anomalies of the PDO, it seems to fail upon the inclusion of SST anomalies in the South Pacific in calculating the IPO. Two other models, GISS-E2-1-H and IPSL-CM6A-LR, also have the wrong sign of the signal in the South Pacific.

d. *Integrative model evaluation*

Here, we quantify the spatiotemporal accuracy of each model in reproducing observed features of the PDO and IPO. To do this, we calculate indices to evaluate model PDOs and IPOs beyond pattern correlations: the representation of the decadal band (20–50 years) within the power spectra, the ratio of tropical-to-extratropical magnitudes in the SST patterns, and the accuracy and magnitude of the spatial pattern (see section 2 for details of these calculations). These three indices were chosen to synthesize a comprehensive set of PDO/IPO features that capture distinctive spatial and temporal aspects of the modes of variability.

In the 16 models analyzed here for both the PDO and IPO, every model underrepresents decadal variability; that is, the percentile of observed decadal power within the model distribution is above the median (Fig. 6, data in Table S1). For five models' PDOs (CNRM-CM6-1, CNRM-ESM2-1, MIROC-ES2L, MIROC6, and MPI-ESM1-2-HR) and 10 models' IPOs (GISS-E2-1-G, GISS-E2-1-H, IPSL-CM6A-LR, CNRM-CM6-1, CNRM-ESM2-1, EC-Earth3, MIROC-ES2L, MIROC6, MPI-ESM1-2-LR, and NorCPM1), the observed decadal power density lies outside of the model distribution of power densities entirely, so no ensemble members are able to reproduce the decadal temporal variability found in the observations. For every model but CanESM5 (15/16 models), the observed PDO decadal power is in the fourth quartile of the model distribution of decadal power. For every model, the observed IPO decadal power is in the fourth quartile of the model distribution (Table S1 and Fig. S7).

Most (12/16) of the models analyzed here have too weak a tropical signal in their PDO, with the exceptions being MIROC6, MIROC-ES2L, GISS-E2-1-G, and CESM2, which have too strong of a tropical signal (in that order) compared to their North Pacific variability. These models also tend to underestimate decadal temporal variability compared to observations. For INM-CM5-0, the tropical-to-North Pacific ratio in the PDO is over 5 times smaller than in observations. This model also has the lowest corrected pattern correlation for both the PDO and IPO ($r' = 0.41$ and 0.28) of all models. Of course, pattern correlations are not independent of the tropical–extratropical signal ratio error, since a model such as INM-CM5-0 with virtually no PDO fingerprint in the tropical Pacific will score poorly in both indices. Thus, in Fig. 6, models with greater equatorial Pacific—North Pacific (EP/NP) relative signal error tend to have low pattern correlations. Some high-correlating models for uncorrected pattern correlations with observed PDOs (CESM2 and MIROC6) have much too strong an overall signal in the Pacific, leaving UKESM1-0-LL with the closest magnitude-corrected representation of the observed global PDO pattern. For the IPO, most models have too much of a tropical signal relative to the extratropical signal, with CanESM5 standing out with a particularly outsized tropical–extratropical ratio compared to models despite this model performing well at this metric for the PDO. Several models that well represent the tropical Pacific in their PDOs overrepresent the tropical Pacific in their IPOs (CanESM5 and IPSL-CM6A-LR). The discrepancy between model PDO versus IPO fidelity in this metric is likely due to the explicit inclusion of the equatorial and South Pacific in the calculation of the IPO.

No models clearly succeed in all three metrics across both the PDO and the IPO. CanESM5 has the best representation

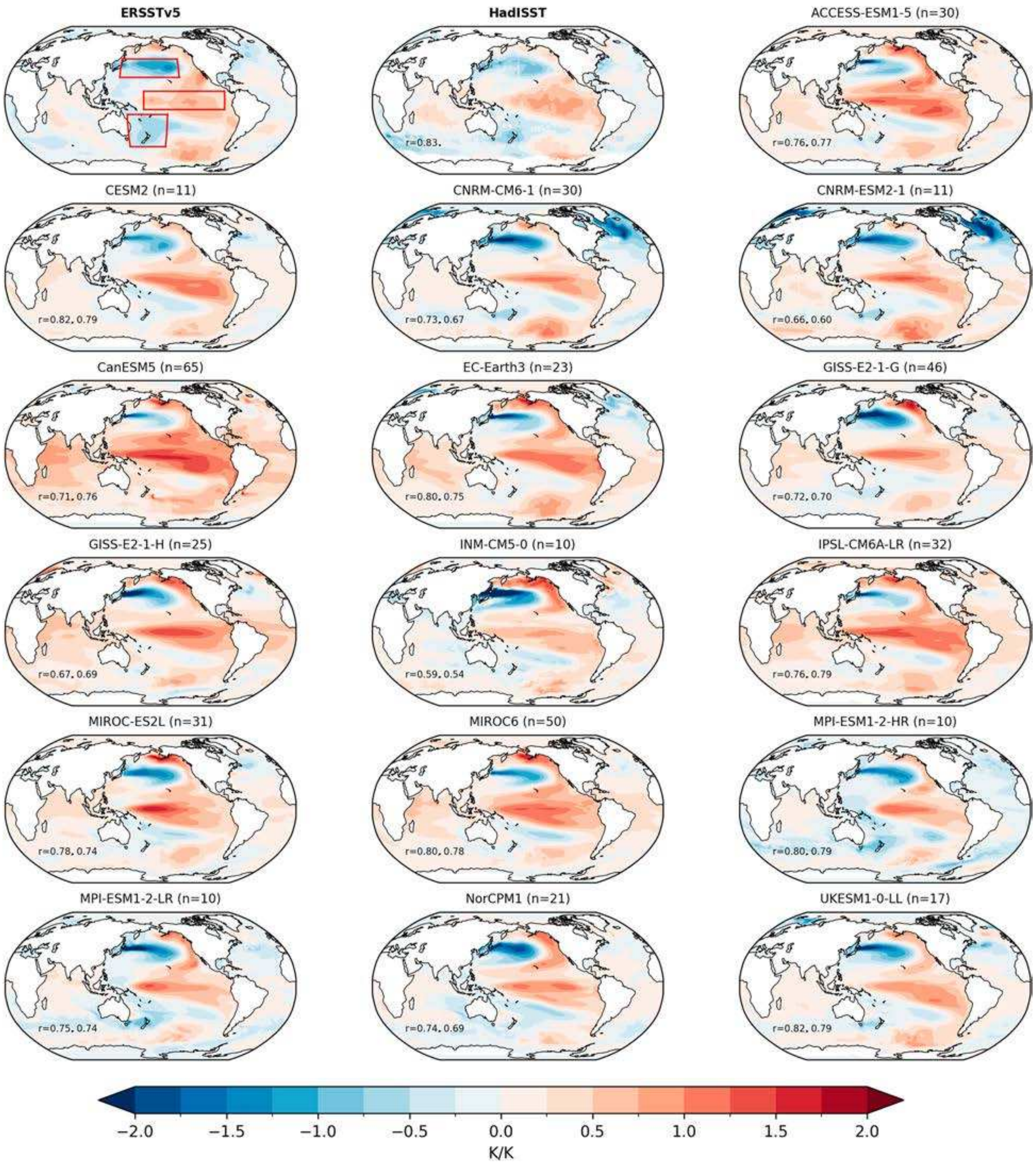

FIG. 4. As in Fig. 1, but for the TPI of the IPO, with regions used to calculate the TPI outlined in red.

of both decadal temporal PDO variability and strength of the tropical–extratropical PDO representation, though it comes seventh out of the models in its corrected pattern correlation for the PDO, 15th for corrected pattern correlation of the IPO, and last for tropical–extratropical IPO representation. On the other hand, while INM-CM5-0 is the worst-ranked model in the spatial indices, it has an acceptable representation of decadal temporal variability. The models that consistently perform poorly for all metrics were MIROC6 and MIROC-ES2L, despite having high uncorrected pattern correlations ($r = 0.89$ and 0.83, respectively), due to their general overrepresentation of the tropical Pacific in PDO metrics and their underrepresentation of decadal variability. Across all three metrics and both the PDO and the IPO, UKESM1-0-LL performs best in total

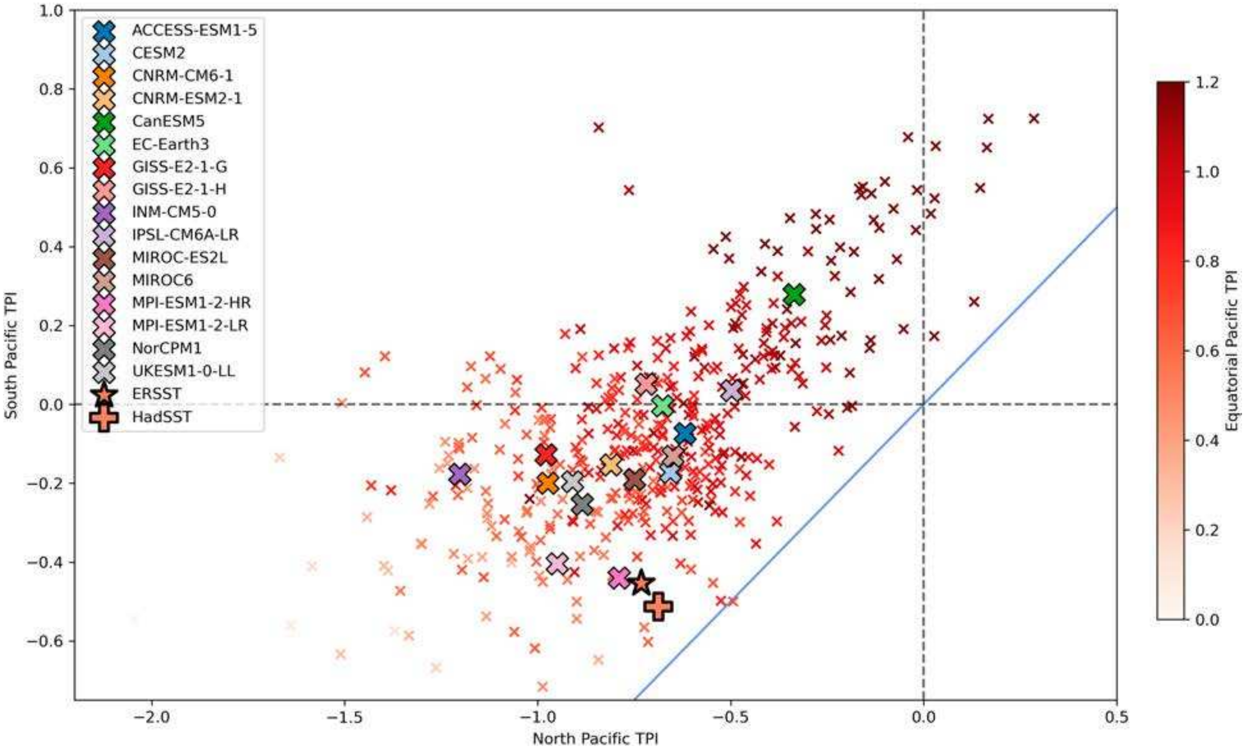

FIG. 5. For each CMIP6 model run (small crosses), model ensemble mean (large crosses), ERSSTv5 (large star), and HadISST (large plus symbol), weighted box averages of the IPO pattern as in Fig. 4 in the TPI regions of the North Pacific (*x* axis), South Pacific (*y* axis), and equatorial Pacific (color on small crosses and observations). The blue line represents the 1:1 line of equal amplitude in the North and South Pacific. All units are kelvin per kelvin (K/K) of the TPI.

rank. While pattern correlations with observations are an important metric by which modeled modes of climate variability are evaluated, our comprehensive comparison of models to observations by several metrics shows that the models with the highest pattern correlations can have the lowest fidelity by other measures.

4. Pacific–hydroclimate teleconnections

Natural decadal variability of Pacific SSTs is closely linked to decadal variability and change in hydroclimate across the globe. Thus, we evaluate the overall ability of CMIP6 models to recreate the observed relationships between the PDO/IPO and hydroclimate variables. We focus on the teleconnections

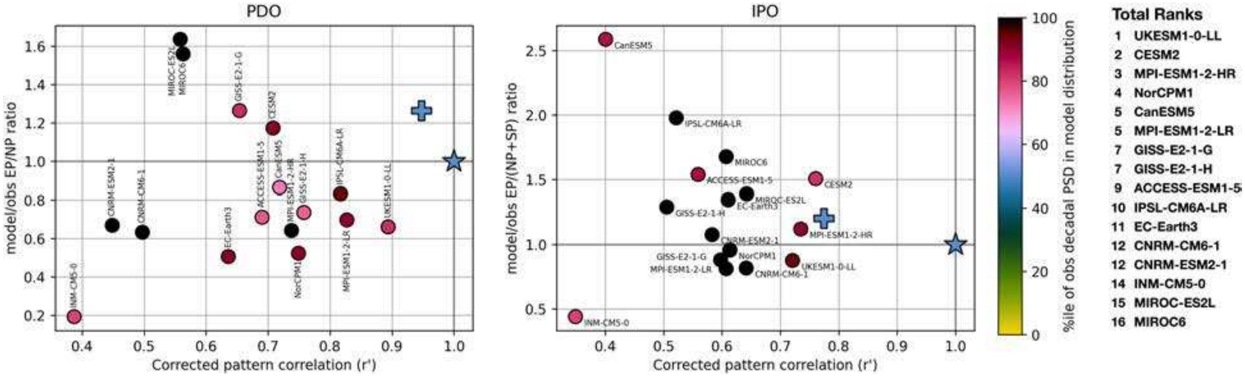

FIG. 6. Model fidelity in representing three key (left) PDO and (right) IPO spatiotemporal characteristics: global pattern correlation with observations (ERSSTv5) of model PDO/IPO SSTA patterns corrected for accuracy in representing magnitude of the observed pattern in the Pacific (*x* axis), ratio of the strength of model to observed tropical–extratropical relative signal in the PDO/IPO SSTA pattern (*y* axis), and the percentile of the observed decadal-band-averaged (20–50 years) power density within the model distribution of decadal power (colors). Blue star represents ERSSTv5 observations, and blue cross represents HadISST observations. Rankings on the right represent total model performance based on the metrics shown, with details in Table S1.

involving SSTs, atmospheric circulation, precipitation, low clouds, and surface VPD, a measure of atmospheric aridity particularly relevant for forest fire in Pacific-teleconnected regions such as the southwestern United States (Williams et al. 2015a; Seager et al. 2015; Jacobson et al. 2022, 2024).

a. Precipitation and circulation associated with the PDO

In boreal winter (DJF) over the tropical Pacific, the PDO-related circulation aloft is characterized by a Gill-like response with high pressure north and south of the equatorial warming, weaker in models than observations (Fig. 7). The Aleutian low is the most prominent feature over the North Pacific in both models and observations. At the surface as well as aloft, the PDO-related Aleutian low is biased north and westward in models (Fig. 9), possibly related to the westward bias of tropical SST anomalies. The teleconnection aloft extends across the Northern Hemisphere midlatitudes in a Pacific North American (PNA)-like pattern, with a low over the southeastern United States and a high over Greenland. In general, the atmospheric teleconnection in the winter hemisphere is too weak in most models and in the multimodel mean. Many models also fail to capture the tropical Gill-like response with sufficient magnitude or symmetry, particularly models with weak equatorial SST anomalies associated with the PDO in DJF. Models with too strong tropical SST responses, on the other hand (e.g., CESM2, GISS-E2-1-G, and MIROC models), overestimate the strength of the atmospheric signal associated with the PDO globally.

For precipitation over land in DJF, much of Canada, the Pacific Northwest, central–eastern United States, northern South America, southern West Africa, southwestern Africa, northern Borneo, and eastern Australia all experience significant declines in precipitation during the warm tropical Pacific phase of the PDO in observations, while significant increases in precipitation occur in the southwestern United States, Mexico, Brazil and southeast South America, the Mediterranean, Madagascar, and around the Himalayas. In general, in the DJF multimodel mean, the precipitation and circulation patterns are accurately recreated ($r = 0.63$ and $r = 0.94$ for precipitation and z_{300}, respectively), though individual models perform worse than the multimodel mean in pattern correlations with the observed teleconnections. For example, though the multimodel mean precipitation–PDO relationship is the correct sign in southwestern North America, individual models disagree on the sign of the teleconnection in southwestern North America. In the observed teleconnection, the enhanced Aleutian low intensifies the Pacific storm track and increases DJF precipitation in the southwest. However, particularly for models in which the Aleutian low teleconnection is too weak and/or biased too far west (e.g., GISS-E2-1-H, CNRM models, and INM-CM5-0), the PDO–precipitation teleconnection in the southwest is far too weak or the wrong sign. In addition, several models simulate a negative precipitation signal in western Australia that is not observed [e.g., CESM2, CanESM5, MIROC models, and NorCPM1; though this and other discrepancies could be a result of a lack of precipitation data over certain regions, such as central–western Australia (Harris et al. 2020)]. Many models also fail to produce the positive precipitation signal over eastern Brazil, a known teleconnection in observations (Kayano and Andreoli 2007).

In boreal summer (JJA; Fig. 8), the observed atmospheric teleconnection is weaker in the Northern Hemisphere than in DJF, but stronger in the Southern Hemisphere, with a low pressure in the eastern South Pacific and a high pressure to its south, resembling the South Pacific Oscillation (SPO) (You and Furtado 2017). While the multimodel mean is relatively accurate ($r = 0.85$ for z_{300}), individual models have mixed degrees of fidelity in simulating the atmospheric PDO teleconnection in JJA. Some models have too strong an atmospheric teleconnection in the tropics and North Pacific (e.g., CESM2, GISS models, MIROC models, and MPI-ESM1-2-LR), and some models fail to simulate an SPO-like pattern in the South Pacific (e.g., CNRM models and INM-CM5-0). For both DJF and JJA in the multimodel mean, the modeled PDO-z_{300} teleconnection is too weak in the winter hemisphere and too strong in the summer hemisphere. In addition, in the observed PDO, cool SSTs in the North Pacific in JJA have west and central maxima, with two low pressure maxima on their northern flanks. Most models fail to reproduce this structure, showing instead one large anticyclone. Positive SSTs in the tropical Pacific in JJA extend too far west in several models, a possible cause for some of these models' failure to simulate realistic SPO-like patterns in the eastern South Pacific.

In JJA over land, all models pick up a strong drying signal over the Indian monsoon region and the Himalayas. For most models, this is stronger than the observed relationship, though the overall monsoon drying is consistent with previous work that identifies drying of the Indian monsoon region during the positive PDO phase due to northeasterly winds from the Pacific opposing climatological moisture flow (Krishnan and Sugi 2003; Meehl and Hu 2006; Krishnamurthy and Krishnamurthy 2017). The PDO-related drying in the East Asian summer monsoon region (Yoon and Yeh 2010) is reproduced in most models. Most models also underestimate or fail to show the observed drying of the West African Monsoon region during positive phases of the PDO (Diatta and Fink 2014; Lüdecke et al. 2021). In the ensemble mean in the Northern Hemisphere and South America, the modeled JJA precipitation teleconnection to the cool-North Pacific-phase PDO is too heterogeneously wet. Finally, in observations as well as in the multimodel mean, the SPO-like circulation is related to increased precipitation in JJA over Chile, similar to that along coastal southwestern North America in DJF. As in boreal summer in the North Pacific, models that simulate a circulation teleconnection in the South Pacific that is too weak or too far west (ACCESS-ESM1-5, CNRM models, and INM-CM5-0) also tend to underestimate or fail to capture the wetting in coastal southern South America.

To compare modeled versus observed precipitation–PDO teleconnections over the ocean, we use satellite observations of precipitation from 1979 to onward (Fig. 9). In DJF, the western flank of the warm equatorial Pacific region experiences increased precipitation, surrounded by drying to the west, north, and south. In JJA, a weaker band of positive precipitation is observed across the equatorial Pacific in line with warm but weaker SSTs. In most models, the positive precipitation anomaly in the tropical Pacific is too far west in both DJF and JJA

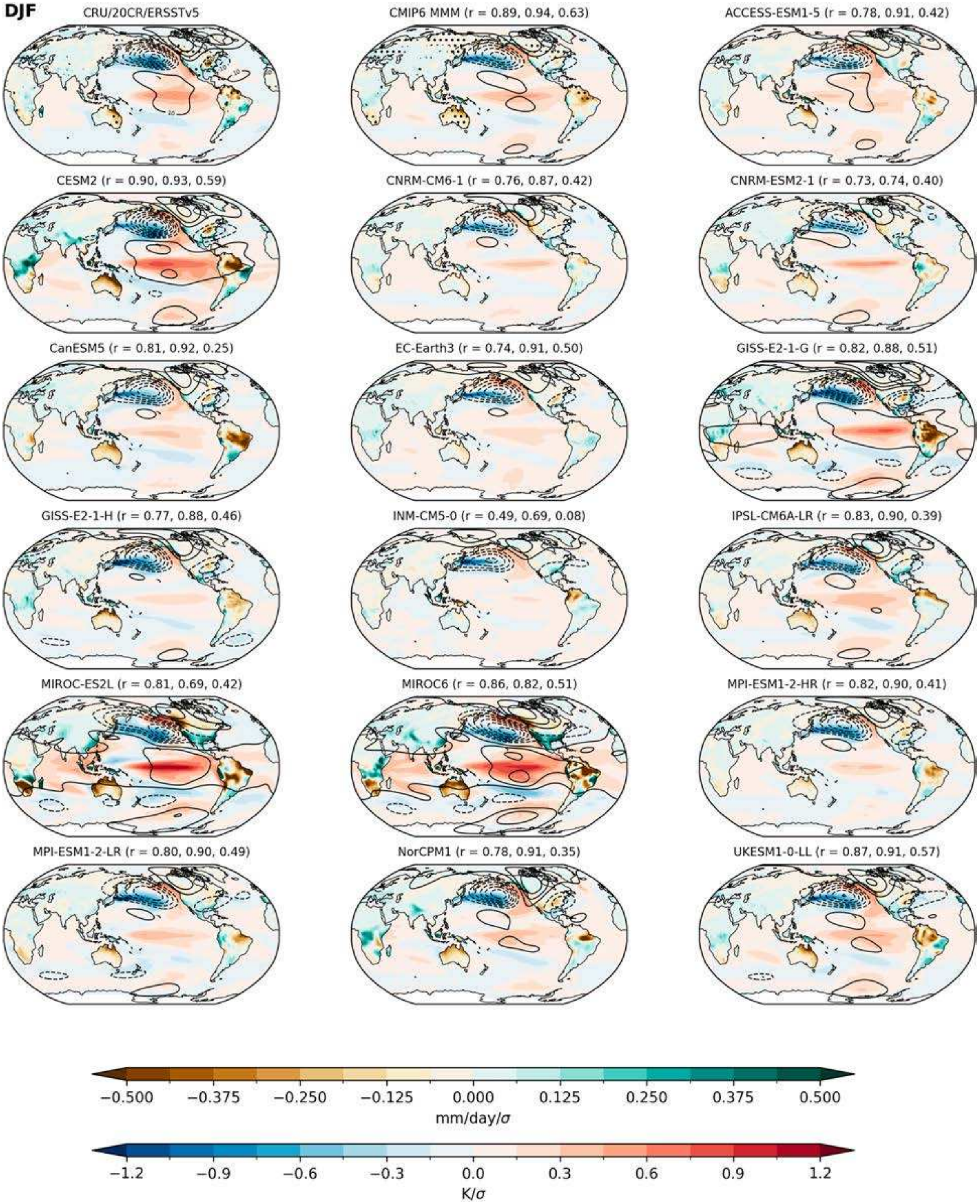

DJF

CRU/20CR/ERSSTv5

CMIP6 MMM (r = 0.89, 0.94, 0.63)

ACCESS-ESM1-5 (r = 0.78, 0.91, 0.42)

CESM2 (r = 0.90, 0.93, 0.59)

CNRM-CM6-1 (r = 0.76, 0.87, 0.42)

CNRM-ESM2-1 (r = 0.73, 0.74, 0.40)

CanESM5 (r = 0.81, 0.92, 0.25)

EC-Earth3 (r = 0.74, 0.91, 0.50)

GISS-E2-1-G (r = 0.82, 0.88, 0.51)

GISS-E2-1-H (r = 0.77, 0.88, 0.46)

INM-CM5-0 (r = 0.49, 0.69, 0.08)

IPSL-CM6A-LR (r = 0.83, 0.90, 0.39)

MIROC-ES2L (r = 0.81, 0.69, 0.42)

MIROC6 (r = 0.86, 0.82, 0.51)

MPI-ESM1-2-HR (r = 0.82, 0.90, 0.41)

MPI-ESM1-2-LR (r = 0.80, 0.90, 0.49)

NorCPM1 (r = 0.78, 0.91, 0.35)

UKESM1-0-LL (r = 0.87, 0.91, 0.57)

FIG. 7. Regression of precipitation (over land; colors), SST (over the ocean; colors), and geopotential height at 300 hPa (globally; contours) anomalies onto PDO time series from 1901 to 2013 in (top left) DJF for observations, (top center) multimodel ensemble mean (MMM), and individual model ensemble means. (top left) The regression of CRU precipitation, ERSSTv5 SST, and 20CR geopotential height at 300-hPa anomalies onto the ERSSTv5 PDO time series. Stippling in (top left) indicates regions where the precipitation regression coefficients are significantly different from zero at the 95% level by a two-sided Student's *t* test. Stippling

(Figs. S8 and S9). In JJA, this equatorial wetting is often erroneously flanked to the north by zonally broad drying.

There is a strong relationship ($r = 0.64$, $p \ll 0.01$) between the closeness of a given model realization's global PDO SST pattern to observations and its ability to simulate accurate precipitation teleconnections over land associated with the PDO (Fig. 10). In terms of these weighted pattern correlations between models and observations in DJF, CESM2 models demonstrate the best fidelity for both precipitation and SSTs, and INM-CM5-0 is the least accurate by both measures by a wide margin. The robust relationship between model ability to simulate precipitation patterns and SST patterns associated with the PDO is evidence that properly simulating spatial patterns of Pacific decadal SST variability is crucial to properly simulating its global hydroclimate teleconnections.

b. *Vapor pressure deficit associated with the PDO*

Figure 11 shows spatial patterns in anomalies of VPD over land related to the PDO. Though the VPD teleconnection patterns are similar to those for precipitation, they differ due to the effects of both atmospheric moisture content and temperature on VPD. VPD teleconnections are generally stronger in the summer hemisphere. Notable regions of observed drying (increased VPD) with a positive PDO in DJF include northwestern North America, northeastern South America, western Australia, southern Africa, and northern Africa/the Sahel into the Arabian Peninsula. With some discrepancies in individual models (Figs. S10 and S11), the multimodel mean captures the pattern across the Americas and southern South Africa but again extends too much drying across to western Australia and lacks consensus on drying in northeastern Africa and the Arabian Peninsula. In DJF, VPD decreases in the positive PDO phase in central Mexico, the eastern United States, and southeastern South America, in both observations and models. In boreal summer (JJA), the positive PDO phase is associated with a decrease in VPD in the western and central United States, the Mediterranean, the Gobi Desert, and northeastern China and an increase in VPD over northeastern South America, eastern North Africa, West Africa, the Horn of Africa, the southern Arabian Peninsula, India, and the northern East Asian summer monsoon region. In JJA, most models simulate the decrease over the United States, the Mediterranean, the Gobi Desert, and northeastern China, but in line with the wet precipitation bias seen in Fig. 8, VPD–PDO relationships in the multimodel mean are too negative across the Northern Hemisphere. In southwestern North America, models that underestimate, or have the incorrect sign of, the boreal winter precipitation–PDO teleconnection (e.g., GISS-E2-1-H, CNRM models, and INM-CM5-0) tend to underestimate the JJA VPD–PDO teleconnection in the southwest. Models simulate the observed increase in VPD in JJA over northeastern South America, India, the southern Arabian Peninsula, West Africa, and northeastern China but disagree with observations in eastern Brazil, Australia, and to some degree northern and central Africa. With some notable biases, the multimodel mean is largely able to replicate VPD and precipitation teleconnections to the PDO across the ocean and land in both DJF and JJA.

c. *Low-level clouds*

In the Pacific, low-level clouds are an important part of the coupling between the atmosphere and the sea surface (Seethala et al. 2015; Clement et al. 2009). Previous work has found that some climate models fail to correctly simulate low-level cloud coverage over the ocean, which in turn can affect their simulations of SST variability and trends over the Pacific and ultimately add to the uncertainty of climate sensitivity to greenhouse gas forcing (Myers and Norris 2015; Cesana and Del Genio 2021). Thus, in Fig. 12, we show the model ensemble means of the CMIP6 model low-cloud–PDO relationship for boreal winter (DJF) and summer (JJA), compared to observations corrected for inhomogeneities (Norris and Evan 2015). In general, the expected low-cloud–PDO relationship would be such that cool SSTs favor increased low-cloud cover and warmer SSTs favor reduced low-cloud cover (Bretherton and Wyant 1997; Seethala et al. 2015; Burgman et al. 2017). The relationship appears to be more complex in both models and observations. Observations indeed indicate a decrease in low-cloud cover in the eastern equatorial Pacific and, in particular, in the eastern subtropical Pacific off Baja California, where the positive PDO phase has warm SSTs in DJF, consistent too with trends in low-cloud anomaly shown in Seethala et al. (2015). The multimodel mean in DJF largely disagrees with observations in the eastern equatorial Pacific, showing a small increase ($<2\%/\sigma$) in low-cloud cover off the western equatorial coast of South America, where models show a small decrease ($<2\%/\sigma$) in cloud cover with a positive PDO signal. This region is also one in which CMIP5 and CMIP6 models have been shown to disagree with observations on the sign of their marine low-cloud feedback (Myers et al. 2021). Models and observations agree on the spatial pattern in the North Atlantic in DJF, with a dipole pattern that is consistent with surface pressure teleconnections in the North Atlantic (see section 4), albeit with the magnitude of the teleconnection too weak in models by approximately a factor of 2. Consistent with our finding that CMIP6 model PDOs produce too weak of a zonal gradient in the equatorial Pacific, we find that models in general fail to capture the zonal asymmetry of the low-cloud–PDO relationship across the tropical and subtropical Pacific but succeed in the extratropical Pacific, with some exceptions.

←

on (top-center) indicates where 14 or more models (>87.5%) agree on the sign of the precipitation teleconnection. The r values shown in parentheses after model names represent the weighted pattern correlations between observations and models for precipitation over land, SST over the ocean, and geopotential height at 300 hPa globally, in that order.

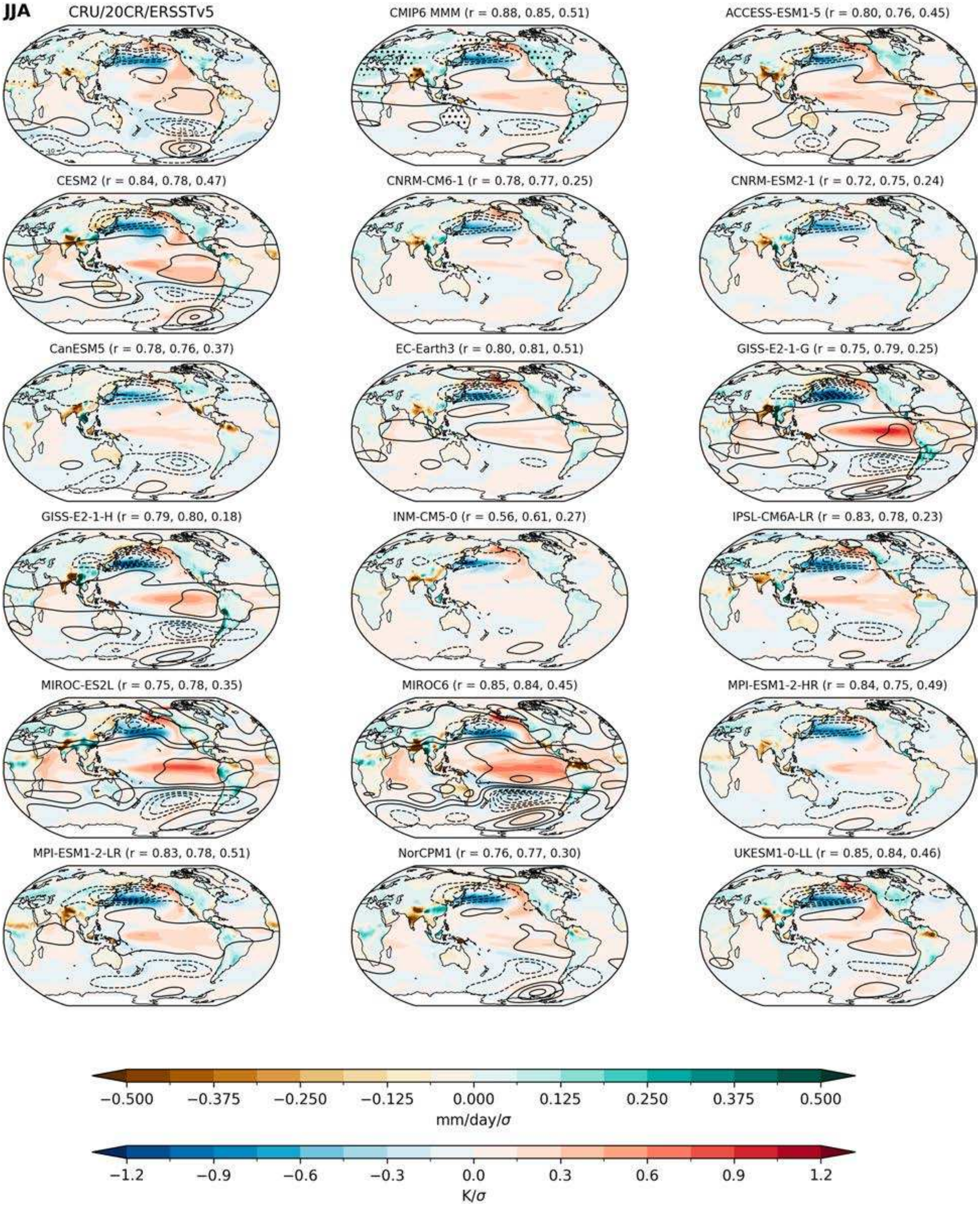

FIG. 8. As in Fig. 7, for anomalies of precipitation (over land; colors), SST (over the ocean; colors), and geopotential height (contours) at 300 hPa regressed onto the PDO time series from 1901 to 2014 in JJA.

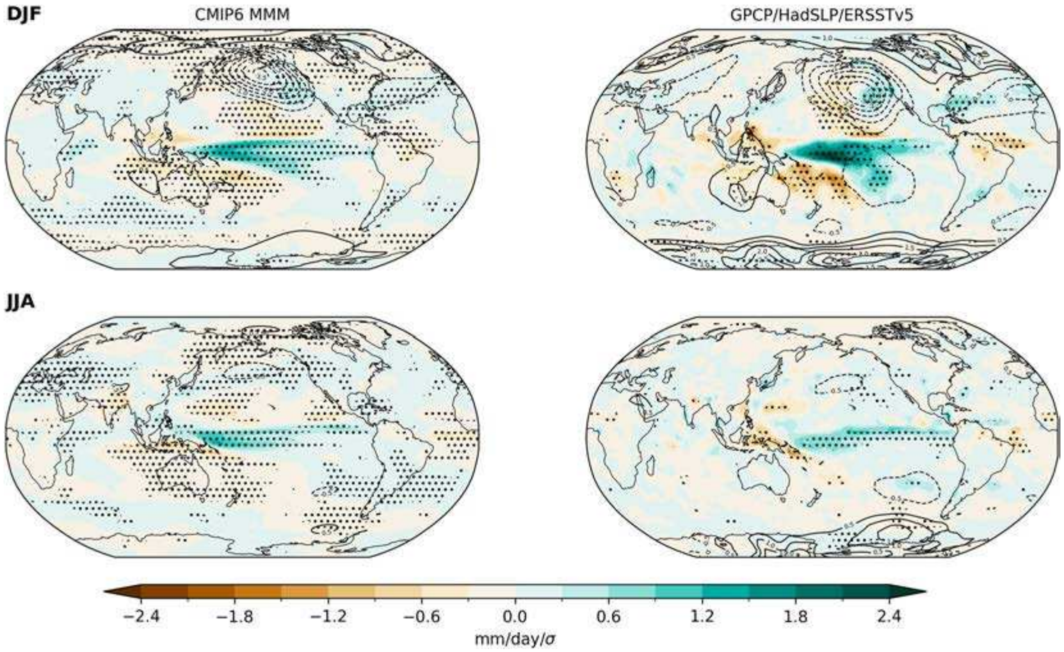

FIG. 9. Multimodel ensemble-mean regression of global precipitation (colors) and sea level pressure (contours) anomalies onto PDO time series from (top) 1979 to 2013 (DJF) and (bottom) 1979–2014 (JJA). Stippling on the left over land indicates where 14 or more models (>87.5%) agree on the sign of the precipitation teleconnection. (right) The regression of seasonal GPCP precipitation and HadSLP sea level pressure anomalies onto the ERSSTv5 PDO time series. Stippling on the right indicates regions where the precipitation regression coefficients are significantly different from zero at the 95% level by a two-sided Student's *t* test.

d. *Teleconnections with the IPO*

Circulation and precipitation anomalies associated with the IPO are similar to those associated with the PDO, with some differences (Figs. 13 and 14). In DJF, observed circulation anomalies have a similar Gill-like response to the equatorial warming and are more hemispherically symmetric, with a low pressure in the south-central Pacific and a high pressure over the Southern Ocean. In the Northern Hemisphere in DJF, the Aleutian low is part of a circumglobal wave train (which is not present in the PDO regressions). All CMIP6 models analyzed except for INM-CM5-0 are able to simulate the Gill-like response in the subtropics, the Aleutian low, and a high pressure over western Canada. Most models do not simulate the full-wave response in the high latitudes. Most models correctly simulate many of the precipitation teleconnections in DJF which are similar to those for the PDO, with many of the same discrepancies with observations as described in section 4: Several models (e.g., ACCESS-ESM1-5 and CanESM5) lack the increased precipitation over eastern Brazil and produce a spurious drying teleconnection in western Australia. In JJA, the observed circulation signal is weaker and concentrated in the Southern Hemisphere in a pattern very similar to that associated with the PDO (Fig. 8). Notably, models that struggle to capture the atmospheric teleconnection with the PDO in the South Pacific in JJA, such as CNRM-ESM2-1 and INM-CM5-0, do seem to simulate an SPO-like pattern associated with the IPO. As with the PDO, modeled precipitation teleconnections to the IPO in JJA have a wet bias in the multimodel mean across South America, western North America, and Europe. In general, IPO hydroclimate teleconnections and model biases therein are similar to those for the PDO; the inclusion of the South Pacific in the IPO does not appear to improve model biases in precipitation across Southern Hemisphere land although it does improve some individual model biases in South Pacific atmospheric teleconnections.

5. Implications for southwestern North America precipitation

Decadal precipitation variability in southwestern North America is closely related to decadal SST variability in the Pacific (Huang et al. 2005; Seager et al. 2005; Dai 2013b; Seager 2016; Seager et al. 2023). The warm (cool) equatorial phases of the PDO and IPO are associated with a cyclonic (anticyclonic) anomaly over the North Pacific leading to increased (decreased) precipitation across the southwestern United States (Figs. 7 and 13). As we have shown that CMIP6 models consistently underestimate the variability of their PDO indices in the decadal (20–50 year) band (Fig. 3), there are likely associated biases in their representation of decadal precipitation variability in the southwestern North America.

Figure 15 shows the positive relationship in both models and observations between trends in Pacific decadal SST indices and water-year (October–September) precipitation in southwestern North America (24°–40°N, 105°–125°W). While models correctly simulate the sign and strength of this relationship,

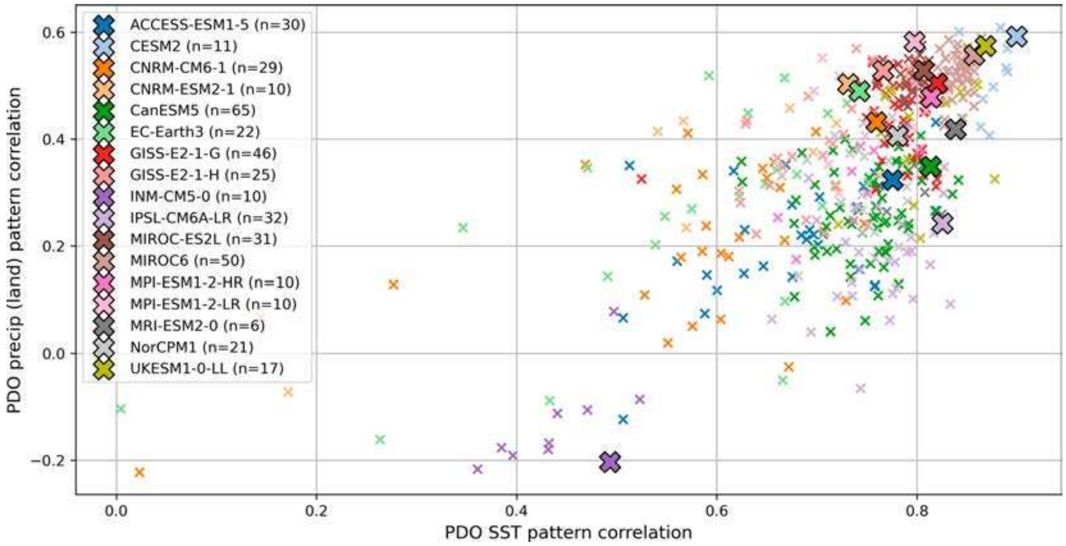

FIG. 10. For each CMIP6 model run (small crosses) and model ensemble mean (large crosses), the weighted pattern correlation between the modeled and observed DJF precipitation patterns over land associated with the PDO (y axis) and the weighted pattern correlation between the modeled and observed DJF SST patterns associated with the PDO (x axis).

they are virtually unable to reproduce the magnitude of the observed maximum and minimum precipitation trends in the southwest. In the 30 years with the most negative trend in observations, 1982–2011, water-year precipitation declined by nearly 30% in the southwest, aligning with the most negative 30-yr trend in the observed PDO index, of nearly 2σ. The observed 1982–2011 precipitation trend is well below the 1st percentile of modeled precipitation trends in the southwest. The

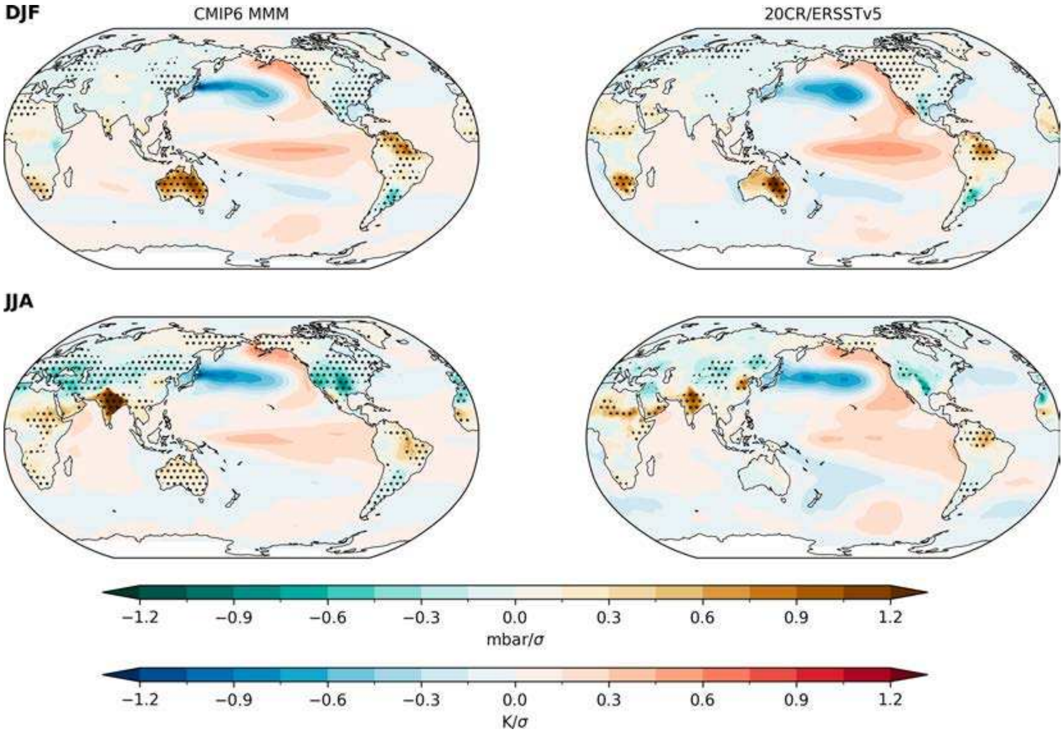

FIG. 11. As in Fig. 9, but for regressions of VPD over land and SSTs over the ocean onto PDO time series and regressions calculated from (top) 1901 to 2013 (DJF) and (bottom) 1901–2014 (JJA).

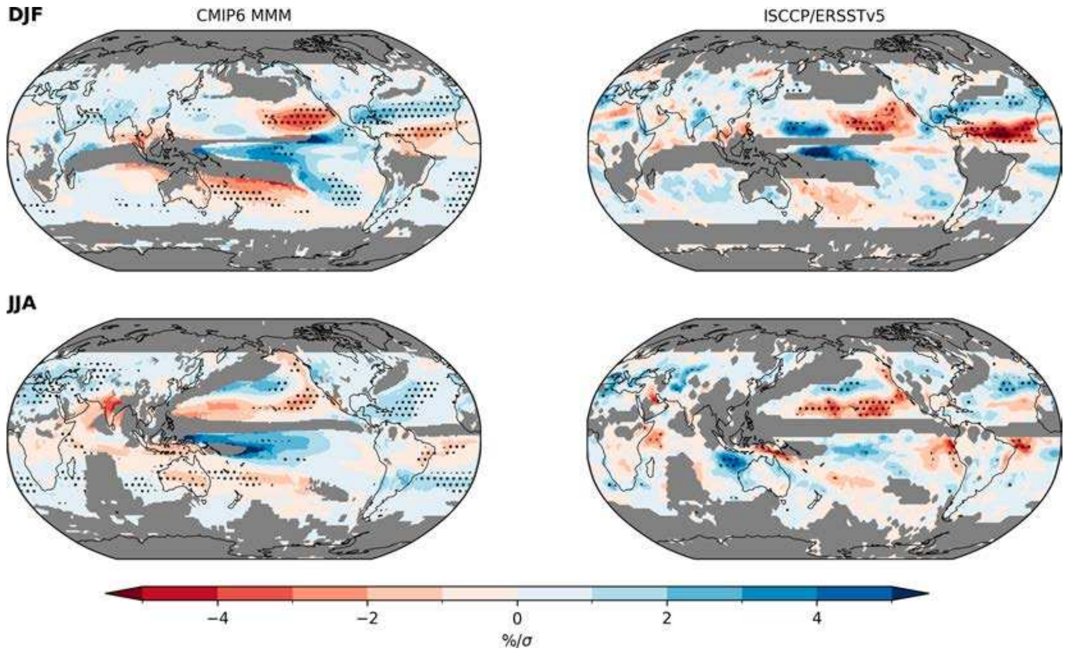

FIG. 12. Multimodel ensemble-mean regression of low-cloud anomalies onto PDO time series from (top) 1984 to 2008 (DJF) and (bottom) 1984–2009 (JJA). Stippling indicates where 14 or more models (>87.5%) agree on the sign of the teleconnection. (right) The regression of ISCCP low-cloud anomalies onto the ERSSTv5 PDO time series. Gray regions indicate where all CMIP6 models and ISCCP data indicate no low-level cloud coverage in the region (see methods).

period with the strongest wetting trend in southwest North America, 1954–83, coincides with a positive (but not extremely so) trend in the PDO and IPO. This positive precipitation trend is in the 99.5th percentile of modeled precipitation trends. The thresholds for the extreme quantiles of observed trends in precipitation, PDO, and IPO correspond with even more extreme quantiles in models: The 5th–95th-percentile range of observed southwest precipitation trends corresponds to, in the model distribution, the 1.5th–98.9th range. For PDO trends, the 5th–95th-percentile range of observed trends corresponds with the 3.5th–95.3rd-percentile range in models. The difference in extreme trends in the IPO is even more apparent, with the 5th–95th-percentile range of observed trends corresponding with the 0.4th–98.1st-percentile range.

The extremeness of these observed precipitation trends within the model distribution is consistent with underestimated natural SST variability on decadal time scales in models (Fig. 3 and Fig. S7) and underestimated Southwest precipitation variability on decadal time scales (Fig. S14). No individual models are able to represent the observed 5th percentile of precipitation trends (Fig. S15). While there is not a significant relationship between decadal-band PDO/IPO power and extreme Southwest precipitation trend representation, some models that represent decadal-band PDO and IPO power within their model distribution (such as CanESM5 and UKESM1-0-LL) have less of a bias in simulating these extreme precipitation trends. Additionally, while modeled trends in Southwest precipitation and Pacific decadal indices have relatively normal distributions about 0, observed trends in these quantities have a larger spread with bimodal distributions in the PDO and precipitation (Fig. 15). Although many possible factors can influence model precipitation trends, these results at least suggest that a possible consequence of models' underestimation of decadal variability of SSTs in the Pacific is their underestimation of decadal variability of hydroclimate in teleconnected land regions and therefore a possible underestimate of the uncertainty due to natural variability of future projections of hydroclimate change.

Finally, while models are generally unable to capture the magnitude of observed extreme precipitation trends in the southwest, these extreme observations and their associated PDO/IPO trends still lie approximately on the axis of the PDO/IPO–precipitation trend relationship simulated by models. This is in contrast with the same results for the PDO/IPO–VPD trend relationships (Fig. S16), which, in agreement with Simpson et al. (2024), demonstrate that modeled VPD trends in the southwest are negatively shifted compared to observed trends. The authors of Simpson et al. (2024) suggest that this bias is most likely due to a model overestimation of the forced thermodynamic increase in vapor pressure with warming, causing a positive shift in the spectrum of modeled vapor pressure trends (and a negative shift in VPD trends) in the southwest.

6. Discussion and conclusions

We have characterized the spatial and temporal representation of Pacific decadal variability in CMIP6 models and

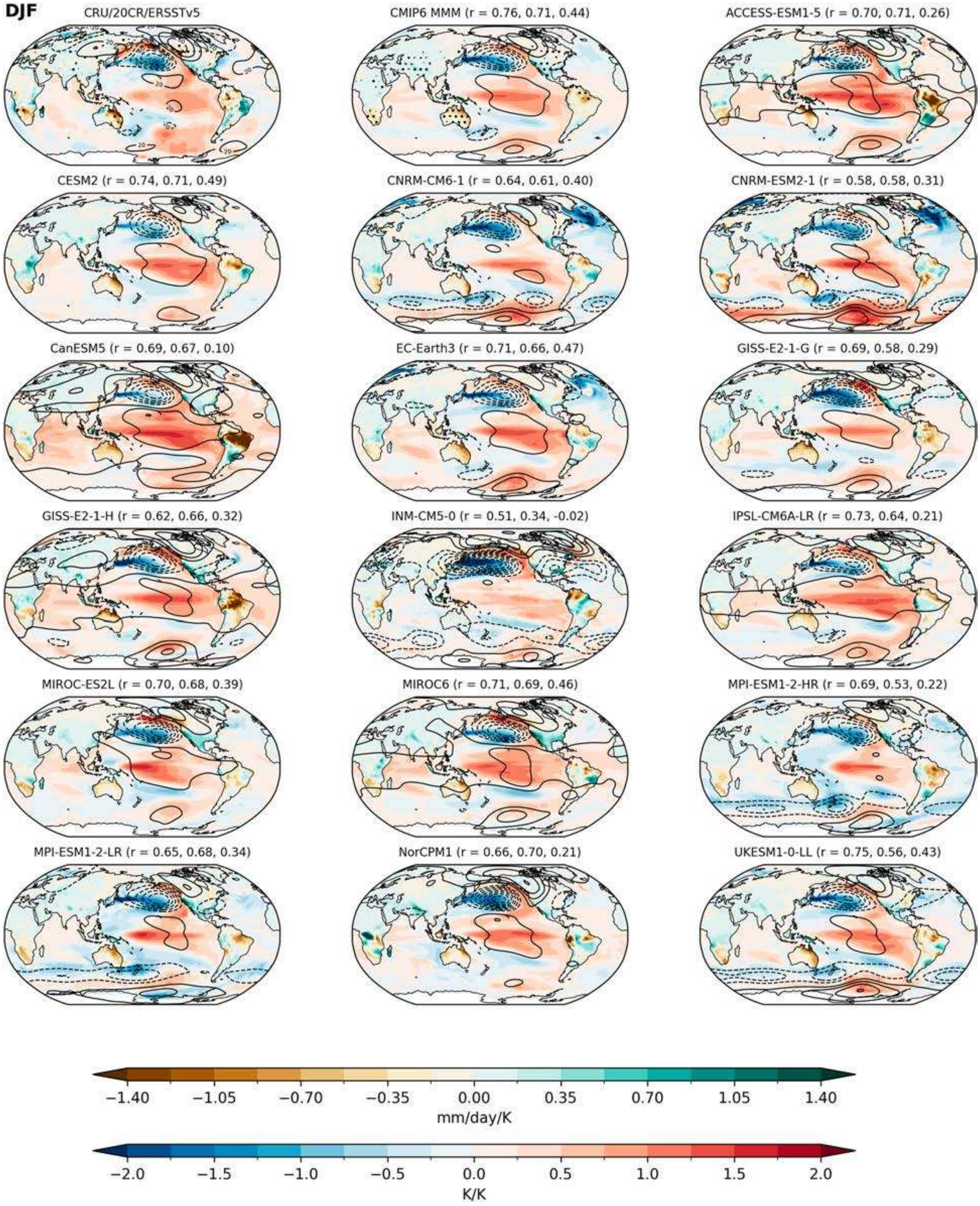

FIG. 13. As in Fig. 7, for anomalies of precipitation (over land; colors), SST (over the ocean; colors), and geopotential height (contours) at 300 hPa regressed onto the TPI of the IPO. Regressions are calculated over 1901–2006 (DJF) due to edge effects of low-pass filtering in the TPI calculation.

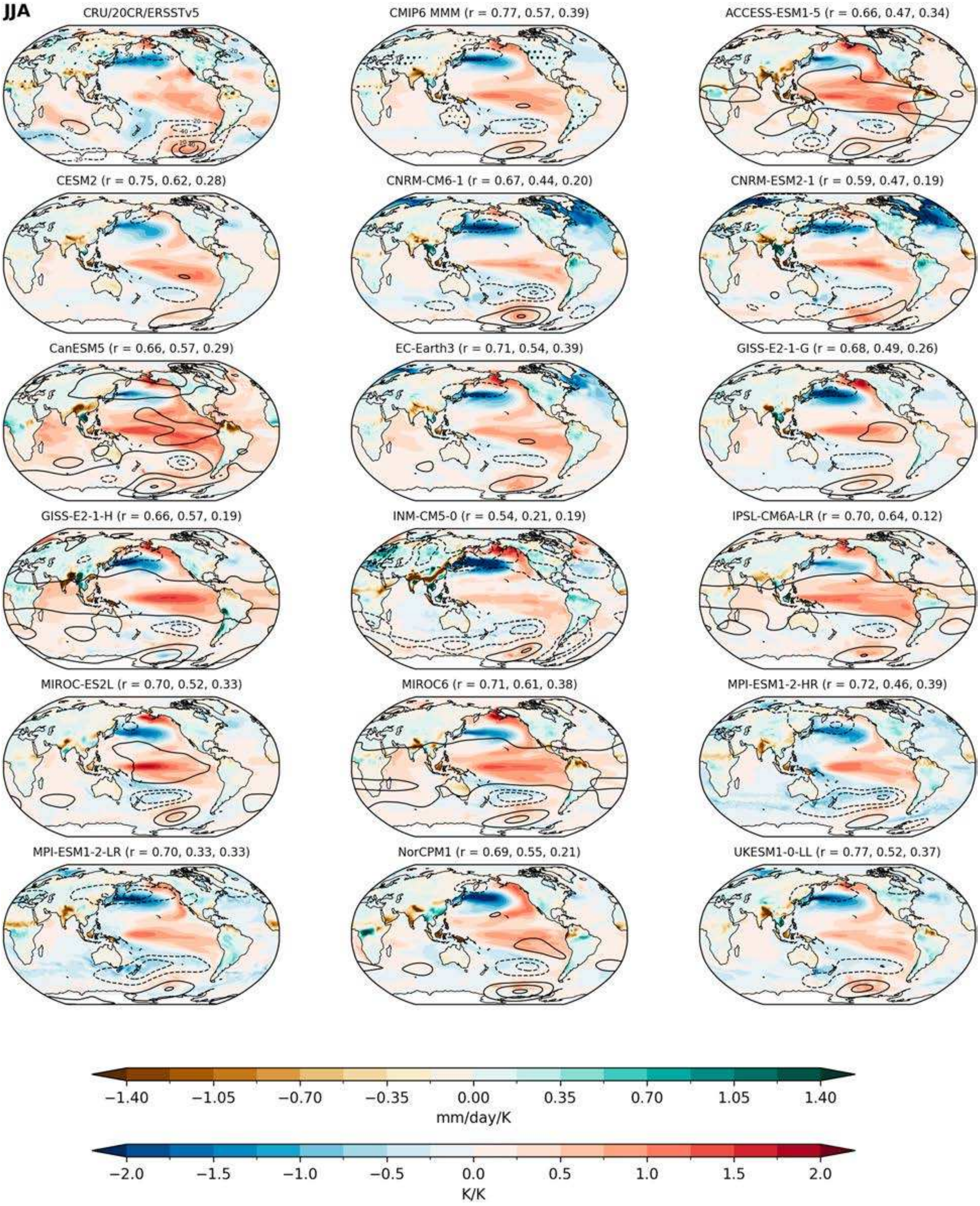

FIG. 14. As in Fig. 13, for anomalies of precipitation (over land; colors), SST (over the ocean; colors), and geopotential height (contours) at 300 hPa regressed onto the TPI of the IPO for 1901–2007 in JJA.

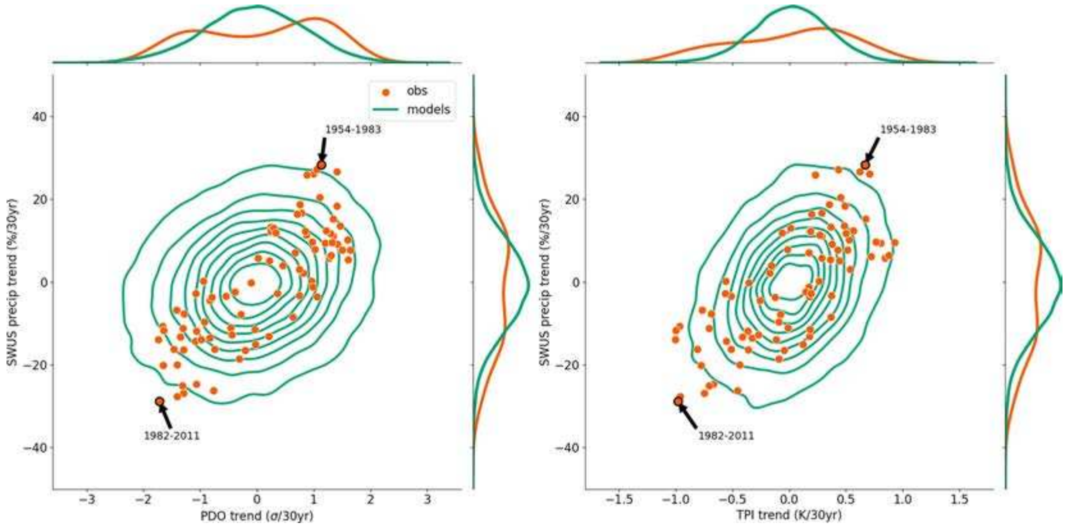

FIG. 15. Distributions of 30-yr trends in (left) the PDO index (*x* axis), (right) the TPI of the IPO (*x* axis), and water-year precipitation in southwestern North America (*y* axis; both) over 1871–2013 (models) and 1902–2013 (observations). The distribution from CMIP6 models is shown as a green contoured bivariate KDE, and observations (CRU) are orange scatter points. The marginal axes show single-variable KDEs for each of the axis variables for models (green) and observations (orange). The 30 years with the wettest and driest precipitation trends in the southwest are labeled.

assessed them based on observations, focusing on the Pacific decadal oscillation and the interdecadal Pacific oscillation. We then evaluated the overall ability of CMIP6 models to reproduce observed teleconnections between Pacific decadal SST variability and global hydroclimate. Finally, we investigated the consequences of models' temporal biases in the Pacific on reproducing precipitation variability in southwestern North America, a region highly influenced by Pacific SSTs. Our main conclusions are as follows, presented using the warm tropic (positive) phase of PDO:

- All 16 models we assessed are able to recreate a PDO pattern close to observations. Most models have a westward bias in their North Pacific cool anomalies, placing the greatest SST anomaly associated with the PDO in the KOE region. Most models also have a too negative west–east gradient in the North Pacific, with too large of a western/central cool anomaly, too weak of an eastern warm anomaly, or both. Most model PDOs have a too weak west–east equatorial gradient in the Pacific due to the warm anomalies being too weak and/or too far west. Most models also have too weak spatial variance in the equatorial Pacific and too strong spatial variance in the North Pacific, while models that are able to simulate strong variance in the equatorial Pacific also overestimate the variance in the North Pacific.
- Models generally recreate the correctly shaped power spectrum of the PDO and IPO, but all models underestimate variability in the 20–50-yr (decadal) band compared to observations. In several models, the observed decadal power density of the PDO and IPO is entirely outside of the ensemble's distribution of power densities.
- Model IPO spatial patterns are similar to observations with some consistent biases. Similar to model PDOs, model IPOs preferentially place the maximum cooling variability in the North Pacific too far west, in the KOE region as opposed to in the central North Pacific. Models have too weak of an IPO signal in the South Pacific compared to the North Pacific. Model biases in circulation and precipitation teleconnections to the PDO are not notably worse or better than those for teleconnections to the IPO.
- Using three metrics [corrected pattern correlation, relative extratropical–tropical pattern magnitude, and decadal (20–50-yr) temporal variability] to quantify models' spatiotemporal representation of the PDO and IPO compared to observations, we find that no models clearly succeed in all facets of simulating Pacific decadal variability. Models with relatively high pattern correlations ($r \sim 0.8$–0.9) between their PDO/IPO patterns and observed patterns still fail in simulating the correct decadal variability and relative magnitudes of tropical-to-extratropical variability. Thus, we emphasize the importance of a multifaceted approach to evaluating modes of natural variability in models that goes beyond simple pattern correlation.
- Consistent with model PDO patterns having too weak of an equatorial SST gradient, models fail to capture the zonal asymmetry of the low-cloud–PDO relationship across the tropical and subtropical Pacific.
- Observed hydroclimate anomalies associated with the PDO and IPO are generally reproduced by the CMIP6 multimodel mean, though individual model biases exist in precipitation and circulation that are consistent with biases in their structure and magnitude of SST patterns for the PDO and IPO.
- CMIP6 models are virtually unable to simulate extreme 30-yr precipitation trends in southwestern North America

of observed magnitudes for both wetting and drying. This is consistent with models' inability to simulate the correct distribution of trends in the PDO and the IPO. Model distributions of these trends are typically not broad enough, possibly due to their underpowered SST variability on decadal time scales.

While in this work we primarily assess model fidelity in simulating Pacific decadal variability on a model-by-model basis, understanding why models have certain biases in their PDOs and IPOs is an important pathway for further research. Shared biases in the spatial pattern of the PDO in models may indicate systematic model biases in dynamical processes. The lack of variance in the equatorial Pacific compared to the extratropics in many models (Figs. 1 and 2) could be because 1) models fail to generate sufficient decadal variability internal to the tropics (Emile-Geay and Cane 2009; Power et al. 2021; Capotondi et al. 2023) or 2) modern climate models are not properly simulating the contribution of extratropical forcing to tropical Pacific decadal variability due to biases in ocean dynamical processes (Newman et al. 2016; Zhao et al. 2021; Farneti 2017; Zhao et al. 2023). In regard to the second possibility, models with undersized PDO signals in the tropical Pacific tend to have weak (or opposite-signed) PDO and IPO signals in the South Pacific. This is consistent with recent findings that CMIP6 models underestimate ENSO teleconnections to the Southern Hemisphere due to a westward bias in tropical Pacific-forced circulation anomalies (Fang et al. 2024), which would result in underestimation of model South Pacific variability in their IPOs. Recent work has also found ocean subsurface processes to be an important driver of decadal variability in the South Pacific, so a lack of proper model representation of these processes may lead to the weak South Pacific model variability shown in Figs. 4 and 5 (Lou et al. 2020).

The source of the westward bias of model SST anomalies in the North Pacific deserves further investigation. Examining net ocean surface heat flux in models versus observations indicates that models have large ocean dynamical-induced SST tendencies in the KOE region that are damped by the atmosphere, possibly related to latitudinal shifts of the KOE (Fig. S17). The stronger, farther-westward-reaching surface Aleutian low in models compared to observations (Fig. 9) could allow for modeled westward-propagating oceanic Rossby waves to affect SSTs along the coast of Japan more easily and earlier than in reality (Seager et al. 2001), causing greater-than-observed variability in the KOE region. Recent work has also found that tropical dynamics drive the central North Pacific maxima of the PDO footprint and that empirically removing the influence of the tropical Pacific on North Pacific variability results in KOE variability overtaking the PDO pattern as the dominant pattern of North Pacific variability (Zhao et al. 2021). Thus, models' overrepresentation of KOE variability compared to the central Pacific in their PDOs may be a result of an insufficient sensitivity of the North Pacific to the tropics. This is consistent with our results showing that while the two MIROC models rank poorly in our PDO evaluation metrics largely due to their overemphasis of the equatorial Pacific (Fig. 6), they are the only models that have maximum SST variability in the central North Pacific rather than in the KOE region (Figs. 1 and 7). The underestimation of decadal-band power in model PDOs may have related dynamical causes. Midlatitude air–sea interaction, the propagation of oceanic Rossby waves, and coupling between the extratropical and tropical Pacific are all considered to be critical physical processes for setting the decadal time scale of the PDO, though the pathways by which these processes can add or reduce variance on decadal and other time scales are complex (Zhang and Delworth 2015; Newman et al. 2016; Liu and Di Lorenzo 2018; Di Lorenzo et al. 2023). Model biases in simulating these processes could cause the reduced PDO decadal variance that we find here, and further investigation into the source of these biases is warranted.

In recent years, there has been growing attention toward an apparent "signal-to-noise paradox" in climate models that has been primarily discussed in terms of variability in the Atlantic sector and whether the observed North Atlantic Oscillation trends are forced, rather than due to natural variability (Scaife and Smith 2018). To engage with this idea in the Pacific sector, in Fig. S18, we show time series of the forced responses of the PDO in each model and the grand ensemble mean. The correlations between the observed PDO and model-simulated forced PDOs are mostly positive but not statistically significant at the 95% threshold, although it is noteworthy that the recent trend toward a negative PDO in observations is replicated, albeit with a smaller magnitude, in most models and in the grand ensemble mean. These results are at least suggestive of a possible interaction between the PDO and radiative forcing.

Our results using large ensembles of CMIP6 models also demonstrate the magnitude of spread between realizations from the same model in their spatial and temporal representations of the PDO and IPO. For most of the models we examine in this study, similar to results for the Community Earth System Model–Large Ensemble in Newman et al. (2016), the intramodel spread in spatial PDO patterns is smaller than the intermodel spread of model ensemble means (e.g., Fig. 2 and Figs. S4 and S5). However, this is not true for the CNRM models and EC-Earth3 models in our study. As found in Coburn and Pryor (2021), the distribution of spatial metrics and power spectra for realizations within a given model is such that caution should be exercised before choosing a single realization to represent that model's performance since this could bias the results depending on which realization is selected. In addition, our results showing systematic biases in models' temporal representations of Pacific decadal variability justify the use of synthetic, realistic decadal variability of Pacific SSTs in forcing model runs as in Seager et al. (2023, 2025). Our finding that models are unable to produce decadal precipitation trends in the Southwest as extreme as observed motivates similar studies of other PDO-teleconnected land regions. Characterizing model PDOs and IPOs, common biases, and the implications of these biases will be useful to climate model developers and users of model data. Understanding the accuracies and biases of climate models' representation of decadal variability is key to accurately assessing uncertainty in future projections due to natural variability and possible interactions between forcing and modes of variability.

Acknowledgments. TWPJ was supported by the National Science Foundation Graduate Research Fellowship (DGE-2036197). RS was supported by the National Science Foundation (AGS-2101214 and OCE-2219829) and the National Oceanic and Atmospheric Administration (NA200AR4310379).

Data availability statement. CMIP6 data are freely available through esgf.llnl.gov/. ERSSTv5 is available at psl.noaa.gov/data/gridded/data.noaa.ersst.v5.html. HadISST is available at https://www.metoffice.gov.uk/hadobs/hadisst/. Precipitation data from CRU and GPCP are available at https://crudata.uea.ac.uk/cru/data/hrg/ and https://psl.noaa.gov/data/gridded/data.gpcp.html. Bias-corrected ISCCP data are available at https://rda.ucar.edu/datasets/d741005/. ERA5 data are available at https://cds.climate.copernicus.eu/. 20CR reconstructions are available at https://www.psl.noaa.gov/data/gridded/data.20thC_ReanV3.html, and HADSLP2 is available at https://www.metoffice.gov.uk/hadobs/hadslp2/.

REFERENCES

Adler, R. F., and Coauthors, 2018: The Global Precipitation Climatology Project (GPCP) monthly analysis (new version 2.3) and a review of 2017 global precipitation. *Atmosphere*, **9**, 138, https://doi.org/10.3390/atmos9040138.

Allan, R., and T. Ansell, 2006: A new globally complete monthly Historical Gridded mean Sea Level Pressure dataset (HadSLP2): 1850–2004. *J. Climate*, **19**, 5816–5842, https://doi.org/10.1175/JCLI3937.1.

Bethke, I., and Coauthors, 2019: NCC NorCPM1 model output prepared for CMIP6 CMIP historical. Earth System Grid Federation, accessed 1 February 2024, https://doi.org/10.22033/ESGF/CMIP6.10894.

Boucher, O., and Coauthors, 2018: IPSL IPSL-CM6A-LR model output prepared for CMIP6 CMIP historical. Earth System Grid Federation, accessed 1 February 2024, https://doi.org/10.22033/ESGF/CMIP6.5195.

Bretherton, C. S., and M. C. Wyant, 1997: Moisture transport, lower-tropospheric stability, and decoupling of cloud-topped boundary layers. *J. Atmos. Sci.*, **54**, 148–167, https://doi.org/10.1175/1520-0469(1997)054<0148:MTLTSA>2.0.CO;2.

Burgman, R. J., B. P. Kirtman, A. C. Clement, and H. Vazquez, 2017: Model evidence for low-level cloud feedback driving persistent changes in atmospheric circulation and regional hydroclimate. *Geophys. Res. Lett.*, **44**, 428–437, https://doi.org/10.1002/2016GL071978.

Capotondi, A., C. Deser, A. Phillips, Y. Okumura, and S. M. Larson, 2020: ENSO and Pacific decadal variability in the Community Earth System Model version 2. *J. Adv. Model. Earth Syst.*, **12**, e2019MS002022, https://doi.org/10.1029/2019MS002022.

——, and Coauthors, 2023: Mechanisms of tropical Pacific decadal variability. *Nat. Rev. Earth Environ.*, **4**, 754–769, https://doi.org/10.1038/s43017-023-00486-x.

Cassou, C., Y. Kushnir, E. Hawkins, A. Pirani, F. Kucharski, I.-S. Kang, and N. Caltabiano, 2018: Decadal climate variability and predictability: Challenges and opportunities. *Bull. Amer. Meteor. Soc.*, **99**, 479–490, https://doi.org/10.1175/BAMS-D-16-0286.1.

Cesana, G. V., and A. D. Del Genio, 2021: Observational constraint on cloud feedbacks suggests moderate climate sensitivity. *Nat. Climate Change*, **11**, 213–218, https://doi.org/10.1038/s41558-020-00970-y.

Chen, X., and J. M. Wallace, 2015: ENSO-like variability: 1900–2013. *J. Climate*, **28**, 9623–9641, https://doi.org/10.1175/JCLI-D-15-0322.1.

Clement, A. C., R. Burgman, and J. R. Norris, 2009: Observational and model evidence for positive low-level cloud feedback. *Science*, **325**, 460–464, https://doi.org/10.1126/science.1171255.

Coburn, J., and S. C. Pryor, 2021: Differential credibility of climate modes in CMIP6. *J. Climate*, **34**, 8145–8164, https://doi.org/10.1175/JCLI-D-21-0359.1.

Compo, G. P., and Coauthors, 2011: Twentieth Century Reanalysis Project. *Quart. J. Roy. Meteor. Soc.*, **137**, 1–28, https://doi.org/10.1002/qj.776.

Dai, A., 2013a: Increasing drought under global warming in observations and models. *Nat. Climate Change*, **3**, 52–58, https://doi.org/10.1038/nclimate1633.

——, 2013b: The influence of the inter-decadal Pacific Oscillation on US precipitation during 1923–2010. *Climate Dyn.*, **41**, 633–646, https://doi.org/10.1007/s00382-012-1446-5.

——, 2021: Hydroclimatic trends during 1950–2018 over global land. *Climate Dyn.*, **56**, 4027–4049, https://doi.org/10.1007/s00382-021-05684-1.

Danabasoglu, G., 2019: NCAR CESM2 model output prepared for CMIP6 CMIP historical. Earth System Grid Federation, accessed 1 February 2024, https://doi.org/10.22033/ESGF/CMIP6.7627.

Delworth, T. L., F. Zeng, A. Rosati, G. A. Vecchi, and A. T. Wittenberg, 2015: A link between the hiatus in global warming and North American drought. *J. Climate*, **28**, 3834–3845, https://doi.org/10.1175/JCLI-D-14-00616.1.

Diatta, S., and A. H. Fink, 2014: Statistical relationship between remote climate indices and west African monsoon variability. *Int. J. Climatol.*, **34**, 3348–3367, https://doi.org/10.1002/joc.3912.

Diffenbaugh, N. S., D. L. Swain, and D. Touma, 2015: Anthropogenic warming has increased drought risk in California. *Proc. Natl. Acad. Sci. USA*, **112**, 3931–3936, https://doi.org/10.1073/pnas.1422385112.

Di Lorenzo, E., and Coauthors, 2023: Modes and mechanisms of Pacific decadal-scale variability. *Ann. Rev. Mar. Sci.*, **15**, 249–275, https://doi.org/10.1146/annurev-marine-040422-084555.

Ebbesmeyer, C. C., D. R. Cayan, D. R. McLain, F. H. Nichols, D. H. Peterson, and K. T. Redmond, 1991: 1976 step in the Pacific climate: For observed and simulated ty environmental changes between 1968-1975 and 1977-1984. *Proc. Seventh Annual Pacific Climate (PACLIM) Workshop, April 1990*, Asilomar, CA, California Department of Water Resources, 115–126, https://openpolar.no/Record/ftaquaticcommons:oai:generic.eprints.org:4562.

EC-Earth, 2019: EC-Earth-Consortium EC-Earth3 model output prepared for CMIP6 CMIP historical. Earth System Grid Federation, accessed 1 February 2024, https://doi.org/10.22033/ESGF/CMIP6.4700.

Emile-Geay, J., and M. A. Cane, 2009: Pacific decadal variability in the view of linear equatorial wave theory. *J. Phys. Oceanogr.*, **39**, 203–219, https://doi.org/10.1175/2008JPO3794.1.

Fang, Y., J. A. Screen, X. Hu, S. Lin, N. C. Williams, and S. Yang, 2024: CMIP6 models underestimate ENSO teleconnections in the Southern Hemisphere. *Geophys.*

Res. Lett., **51**, e2024GL110738, https://doi.org/10.1029/2024GL110738.

Farneti, R., 2017: Modelling interdecadal climate variability and the role of the ocean. *Wiley Interdiscip. Rev.: Climate Change*, **8**, e441, https://doi.org/10.1002/wcc.441.

Fleming, L. E., and K. J. Anchukaitis, 2016: North Pacific decadal variability in the CMIP5 last millennium simulations. *Climate Dyn.*, **47**, 3783–3801, https://doi.org/10.1007/s00382-016-3041-7.

Garreaud, R., and D. S. Battisti, 1999: Interannual (ENSO) and interdecadal (ENSO-like) variability in the Southern hemisphere tropospheric circulation. *J. Climate*, **12**, 2113–2123, https://doi.org/10.1175/1520-0442(1999)012<2113:IEAIEL>2.0.CO;2.

Gong, H., L. Wang, W. Chen, D. Nath, G. Huang, and W. Tao, 2015: Diverse influences of ENSO on the east Asian–western Pacific winter climate tied to different ENSO properties in CMIP5 models. *J. Climate*, **28**, 2187–2202, https://doi.org/10.1175/JCLI-D-14-00405.1.

Hajima, T., and Coauthors, 2019: MIROC MIROC-ES2L model output prepared for CMIP6 CMIP historical. Earth System Grid Federation, accessed 1 February 2024, https://doi.org/10.22033/ESGF/CMIP6.5602.

Harris, I., T. J. Osborn, P. Jones, and D. Lister, 2020: Version 4 of the CRU TS monthly high-resolution gridded multivariate climate dataset. *Sci. Data*, **7**, 109, https://doi.org/10.1038/s41597-020-0453-3.

Hegerl, G., and F. Zwiers, 2011: Use of models in detection and attribution of climate change. *Wiley Interdiscip. Rev.: Climate Change*, **2**, 570–591, https://doi.org/10.1002/wcc.121.

Henley, B. J., J. Gergis, D. J. Karoly, S. Power, J. Kennedy, and C. K. Folland, 2015: A tripole index for the interdecadal pacific oscillation. *Climate Dyn.*, **45**, 3077–3090, https://doi.org/10.1007/s00382-015-2525-1.

Hersbach, H., and Coauthors, 2020: The ERA5 global reanalysis. *Quart. J. Roy. Meteor. Soc.*, **146**, 1999–2049, https://doi.org/10.1002/qj.3803.

Huang, B., and Coauthors, 2017: Extended Reconstructed Sea Surface Temperature, version 5 (ERSSTv5): Upgrades, validations, and intercomparisons. *J. Climate*, **30**, 8179–8205, https://doi.org/10.1175/JCLI-D-16-0836.1.

Huang, H.-P., R. Seager, and Y. Kushnir, 2005: The 1976/77 transition in precipitation over the Americas and the influence of tropical sea surface temperature. *Climate Dyn.*, **24**, 721–740, https://doi.org/10.1007/s00382-005-0015-6.

Jacobson, T. W. P., R. Seager, A. P. Williams, and N. Henderson, 2022: Climate dynamics preceding summer forest fires in California and the extreme case of 2018. *J. Appl. Meteor. Climatol.*, **61**, 989–1002, https://doi.org/10.1175/JAMC-D-21-0198.1.

——, ——, ——, I. R. Simpson, K. A. McKinnon, and H. Liu, 2024: An unexpected decline in spring atmospheric humidity in the interior southwestern united states and implications for forest fires. *J. Hydrometeor.*, **25**, 373–390, https://doi.org/10.1175/JHM-D-23-0121.1.

Jiang, W., P. Huang, G. Huang, and J. Ying, 2021: Origins of the excessive westward extension of ENSO SST simulated in CMIP5 and CMIP6 models. *J. Climate*, **34**, 2839–2851, https://doi.org/10.1175/JCLI-D-20-0551.1.

Jungclaus, J., and Coauthors, 2019: MPI-M MPI-ESM1.2-HR model output prepared for CMIP6 CMIP historical. Earth System Grid Federation, accessed 1 February 2024, https://doi.org/10.22033/ESGF/CMIP6.6594.

Kayano, M. T., and R. V. Andreoli, 2007: Relations of South American summer rainfall interannual variations with the Pacific decadal oscillation. *Int. J. Climatol.*, **27**, 531–540, https://doi.org/10.1002/joc.1417.

Kosaka, Y., and S.-P. Xie, 2013: Recent global-warming hiatus tied to equatorial Pacific surface cooling. *Nature*, **501**, 403–407, https://doi.org/10.1038/nature12534.

Krishnamurthy, L., and V. Krishnamurthy, 2017: Indian monsoon's relation with the decadal part of PDO in observations and NCAR CCSM4. *Int. J. Climatol.*, **37**, 1824–1833, https://doi.org/10.1002/joc.4815.

Krishnan, R., and M. Sugi, 2003: Pacific decadal oscillation and variability of the Indian summer monsoon rainfall. *Climate Dyn.*, **21**, 233–242, https://doi.org/10.1007/s00382-003-0330-8.

Lee, H. S., T. Yamashita, and T. Mishima, 2012: Multi-decadal variations of ENSO, the Pacific decadal oscillation and tropical cyclones in the western North Pacific. *Prog. Oceanogr.*, **105**, 67–80, https://doi.org/10.1016/j.pocean.2012.04.009.

Lee, M., T. Kim, D.-H. Cha, S.-K. Min, D.-S. R. Park, S.-W. Yeh, and J. C. Chan, 2021: How does Pacific decadal oscillation affect tropical cyclone activity over far East Asia? *Geophys. Res. Lett.*, **48**, e2021GL096267, https://doi.org/10.1029/2021GL096267.

Lehner, F., S. Coats, T. F. Stocker, A. G. Pendergrass, B. M. Sanderson, C. C. Raible, and J. E. Smerdon, 2017: Projected drought risk in 1.5°C and 2°C warmer climates. *Geophys. Res. Lett.*, **44**, 7419–7428, https://doi.org/10.1002/2017GL074117.

Liu, Z., and E. Di Lorenzo, 2018: Mechanisms and predictability of Pacific decadal variability. *Curr. Climate Change Rep.*, **4**, 128–144, https://doi.org/10.1007/s40641-018-0090-5.

Lou, J., N. J. Holbrook, and T. J. O'Kane, 2019: South Pacific decadal climate variability and potential predictability. *J. Climate*, **32**, 6051–6069, https://doi.org/10.1175/JCLI-D-18-0249.1.

——, T. J. O'Kane, and N. J. Holbrook, 2020: A linear inverse model of tropical and South Pacific seasonal predictability. *J. Climate*, **33**, 4537–4554, https://doi.org/10.1175/JCLI-D-19-0548.1.

Lüdecke, H.-J., G. Müller-Plath, M. G. Wallace, and S. Lüning, 2021: Decadal and multidecadal natural variability of African rainfall. *J. Hydrol.*, **34**, 100795, https://doi.org/10.1016/j.ejrh.2021.100795.

Ma, Y., N. Yuan, T. Dong, and W. Dong, 2023: On the Pacific decadal oscillation simulations in CMIP6 models: A new test-bed from climate network analysis. *Asia-Pac. J. Atmos. Sci.*, **59**, 17–28, https://doi.org/10.1007/s13143-022-00286-1.

Mantua, N. J., and S. R. Hare, 2002: The Pacific Decadal Oscillation. *J. Oceanogr.*, **58**, 35–44, https://doi.org/10.1023/A:1015820616384.

——, ——, Y. Zhang, J. M. Wallace, and R. C. Francis, 1997: A Pacific interdecadal climate oscillation with impacts on Salmon production. *Bull. Amer. Meteor. Soc.*, **78**, 1069–1079, https://doi.org/10.1175/1520-0477(1997)078<1069:APICOW>2.0.CO;2.

Meehl, G. A., and A. Hu, 2006: Megadroughts in the Indian monsoon region and southwest North America and a mechanism for associated multidecadal Pacific Sea surface temperature anomalies. *J. Climate*, **19**, 1605–1623, https://doi.org/10.1175/JCLI3675.1.

Myers, T. A., and J. R. Norris, 2015: On the relationships between subtropical clouds and meteorology in observations and CMIP3 and CMIP5 models. *J. Climate*, **28**, 2945–2967, https://doi.org/10.1175/JCLI-D-14-00475.1.

——, R. C. Scott, M. D. Zelinka, S. A. Klein, J. R. Norris, and P. M. Caldwell, 2021: Observational constraints on low cloud feedback reduce uncertainty of climate sensitivity. *Nat. Climate Change*, **11**, 501–507, https://doi.org/10.1038/s41558-021-01039-0.

NASA/GISS, 2018: NASA-GISS GISS-E2.1G model output prepared for CMIP6 CMIP historical. Earth System Grid Federation, accessed 1 February 2024, https://doi.org/10.22033/ESGF/CMIP6.7127.

——, 2019: NASA-GISS GISS-E2.1H model output prepared for CMIP6 CMIP historical. Earth System Grid Federation, accessed 1 February 2024, https://doi.org/10.22033/ESGF/CMIP6.7128.

Newman, M., and Coauthors, 2016: The Pacific decadal oscillation, revisited. *J. Climate*, **29**, 4399–4427, https://doi.org/10.1175/JCLI-D-15-0508.1.

Nigam, S., M. Barlow, and E. H. Berbery, 1999: Analysis links pacific decadal variability to drought and streamflow in united states. *Eos, Trans.* Amer. Geophys. Union, **80**, 621–625, https://doi.org/10.1029/99EO00412.

Nitta, T., and S. Yamada, 1989: Recent warming of tropical sea surface temperature and its relationship to the Northern Hemisphere circulation. *J. Meteor. Soc. Japan*, **67**, 375–383, https://doi.org/10.2151/jmsj1965.67.3_375.

Norris, J. R., and A. T. Evan, 2015: Empirical removal of artifacts from the ISCCP and PATMOS-x satellite cloud records. *J. Atmos. Oceanic Technol.*, **32**, 691–702, https://doi.org/10.1175/JTECH-D-14-00058.1.

Oshima, K., and Y. Tanimoto, 2009: An evaluation of reproducibility of the Pacific decadal oscillation in the CMIP3 simulations. *J. Meteor. Soc. Japan*, **87**, 755–770, https://doi.org/10.2151/jmsj.87.755.

Power, S., T. Casey, C. Folland, A. Colman, and V. Mehta, 1999: Inter-decadal modulation of the impact of ENSO on Australia. *Climate Dyn.*, **15**, 319–324, https://doi.org/10.1007/s003820050284.

——, and Coauthors, 2021: Decadal climate variability in the tropical Pacific: Characteristics, causes, predictability, and prospects. *Science*, **374**, eaay9165, https://doi.org/10.1126/science.aay9165.

Rayner, N. A., D. E. Parker, E. B. Horton, C. K. Folland, L. V. Alexander, D. P. Rowell, E. C. Kent, and A. Kaplan, 2003: Global analyses of sea surface temperature, sea ice, and night marine air temperature since the late nineteenth century. *J. Geophys. Res.*, **108**, 4407, https://doi.org/10.1029/2002JD002670.

Rieger, N., and S. J. Levang, 2024: xeofs: Comprehensive EOF analysis in Python with xarray. *J. Open Source Software*, **9**, 6060, https://doi.org/10.21105/joss.06060.

Scaife, A. A., and D. Smith, 2018: A signal-to-noise paradox in climate science. *npj Climate Atmos. Sci.*, **1**, 28, https://doi.org/10.1038/s41612-018-0038-4.

Schiffer, R. A., and W. B. Rossow, 1983: The International Satellite Cloud Climatology Project (ISCCP): The first project of the world climate research programme. *Bull. Amer. Meteor. Soc.*, **64**, 779–784, https://doi.org/10.1175/1520-0477-64.7.779.

Seager, R., 2016: Decadal hydroclimate variability across the Americas. *Climate Change: Multidecadal and Beyond*, World Scientific, 235–254.

——, and M. Hoerling, 2014: Atmosphere and ocean origins of North American droughts. *J. Climate*, **27**, 4581–4606, https://doi.org/10.1175/JCLI-D-13-00329.1.

——, and M. Ting, 2017: Decadal drought variability over North America: Mechanisms and predictability. *Curr. Climate Change Rep.*, **3**, 141–149, https://doi.org/10.1007/s40641-017-0062-1.

——, Y. Kushnir, N. H. Naik, M. A. Cane, and J. Miller, 2001: Wind-driven shifts in the latitude of the Kuroshio–Oyashio extension and generation of SST anomalies on decadal timescales. *J. Climate*, **14**, 4249–4265, https://doi.org/10.1175/1520-0442(2001)014<4249:WDSITL>2.0.CO;2.

——, ——, C. Herweijer, N. Naik, and J. Velez, 2005: Modeling of tropical forcing of persistent droughts and pluvials over western North America: 1856–2000. *J. Climate*, **18**, 4065–4088, https://doi.org/10.1175/JCLI3522.1.

——, A. Hooks, A. P. Williams, B. Cook, J. Nakamura, and N. Henderson, 2015: Climatology, variability, and trends in the U.S. vapor pressure deficit, an important fire-related meteorological quantity. *J. Appl. Meteor. Climatol.*, **54**, 1121–1141, https://doi.org/10.1175/JAMC-D-14-0321.1.

——, N. Henderson, and M. Cane, 2022a: Persistent discrepancies between observed and modeled trends in the tropical Pacific Ocean. *J. Climate*, **35**, 4571–4584, https://doi.org/10.1175/JCLI-D-21-0648.1.

——, M. Ting, P. Alexander, J. Nakamura, H. Liu, C. Li, and I. R. Simpson, 2022b: Mechanisms of a meteorological drought onset: Summer 2020 to spring 2021 in southwestern North America. *J. Climate*, **35**, 7367–7385, https://doi.org/10.1175/JCLI-D-22-0314.1.

——, ——, ——, H. Liu, J. Nakamura, C. Li, and M. Newman, 2023: Ocean-forcing of cool season precipitation drives ongoing and future decadal drought in southwestern North America. *npj Climate Atmos. Sci.*, **6**, 141, https://doi.org/10.1038/s41612-023-00461-9.

——, ——, ——, ——, C. Li, and J. Nakamura, 2025: Dynamics of future soil moisture drought in southwest North America: Linkages across seasons in the ocean–atmosphere–land system. *J. Climate*, **38**, 2139–2154, https://doi.org/10.1175/JCLI-D-24-0235.1.

Seethala, C., J. R. Norris, and T. A. Myers, 2015: How has subtropical stratocumulus and associated meteorology changed since the 1980s? *J. Climate*, **28**, 8396–8410, https://doi.org/10.1175/JCLI-D-15-0120.1.

Seferian, R., 2018: CNRM-CERFACS CNRM-ESM2-1 model output prepared for CMIP6 CMIP historical. Earth System Grid Federation, accessed 1 February 2024, https://doi.org/10.22033/ESGF/CMIP6.4068.

Shukla, S., M. Safeeq, A. AghaKouchak, K. Guan, and C. Funk, 2015: Temperature impacts on the water year 2014 drought in California. *Geophys. Res. Lett.*, **42**, 4384–4393, https://doi.org/10.1002/2015GL063666.

Simpson, I. R., K. A. McKinnon, D. Kennedy, D. M. Lawrence, F. Lehner, and R. Seager, 2024: Observed humidity trends in dry regions contradict climate models. *Proc. Natl. Acad. Sci. USA*, **121**, e2302480120, https://doi.org/10.1073/pnas.2302480120.

Swart, N. C., and Coauthors, 2019: CCCma CanESM5 model output prepared for CMIP6 CMIP historical. Earth System Grid Federation, accessed 1 February 2024, https://doi.org/10.22033/ESGF/CMIP6.3610.

Tang, Y., S. Rumbold, R. Ellis, D. Kelley, J. Mulcahy, A. Sellar, J. Walton, and C. Jones, 2019: MOHC UKESM1.0-LL model output prepared for CMIP6 CMIP historical. Earth System Grid Federation, accessed 1 February 2024, https://doi.org/10.22033/ESGF/CMIP6.6113.

Tatebe, H., and M. Watanabe, 2018: MIROC MIROC6 model output prepared for CMIP6 CMIP historical. Earth System Grid Federation, accessed 1 February 2024, https://doi.org/10.22033/ESGF/CMIP6.5603.

Trenberth, K. E., 1990: Recent observed interdecadal climate changes in the Northern Hemisphere. *Bull. Amer. Meteor. Soc.*, **71**, 988–993, https://doi.org/10.1175/1520-0477(1990)071<0988:ROICCI>2.0.CO;2.

Venrick, E. L., J. A. McGowan, D. R. Cayan, and T. L. Hayward, 1987: Climate and chlorophyll a: Long-term trends in the Central North Pacific Ocean. *Science*, **238**, 70–72, https://doi.org/10.1126/science.238.4823.70.

Vishnu, S., P. A. Francis, S. C. Shenoi, and S. S. V. S. Ramakrishna, 2018: On the relationship between the Pacific decadal oscillation and monsoon depressions over the Bay of Bengal. *Atmos. Sci. Lett.*, **19**, e825, https://doi.org/10.1002/asl.825.

Voldoire, A., 2018: CMIP6 simulations of the CNRM-CERFACS based on CNRM-CM6-1 model for CMIP experiment historical. Earth System Grid Federation, accessed 1 February 2024, https://doi.org/10.22033/ESGF/CMIP6.4066.

Volodin, E., and Coauthors, 2019: INM INM-CM5-0 model output prepared for CMIP6 CMIP historical. Earth System Grid Federation, accessed 1 February 2024, https://doi.org/10.22033/ESGF/CMIP6.5070.

Wang, L., X. Gu, L. J. Slater, J. Li, D. Kong, X. Zhang, and J. Liu, 2023: Phase shifts of the PDO and AMO alter the translation distance of global tropical cyclones. *Earth's Future*, **11**, e2022EF003079, https://doi.org/10.1029/2022EF003079.

Wang, S., and R. Toumi, 2021: Recent migration of tropical cyclones toward coasts. *Science*, **371**, 514–517, https://doi.org/10.1126/science.abb9038.

Wang, T., and J.-P. Miao, 2018: Twentieth-century Pacific decadal oscillation simulated by CMIP5 coupled models. *Atmos. Oceanic Sci. Lett.*, **11**, 94–101, https://doi.org/10.1080/16742834.2017.1381548.

Wang, X., C. Wang, L. Zhang, and X. Wang, 2015: Multidecadal variability of tropical cyclone rapid intensification in the western North Pacific. *J. Climate*, **28**, 3806–3820, https://doi.org/10.1175/JCLI-D-14-00400.1.

Wei, Y., H. Yu, J. Huang, Y. He, B. Yang, X. Guan, and X. Liu, 2018: Comparison of the Pacific decadal oscillation in climate model simulations and observations. *Int. J. Climatol.*, **38**, e99–e118, https://doi.org/10.1002/joc.5355.

Wen, C., A. Kumar, and Y. Xue, 2014: Factors contributing to uncertainty in Pacific decadal oscillation index. *Geophys. Res. Lett.*, **41**, 7980–7986, https://doi.org/10.1002/2014GL061992.

Wieners, K.-H., and Coauthors, 2019: MPI-M MPI-ESM1.2-LR model output prepared for CMIP6 CMIP historical. Earth System Grid Federation, accessed 1 February 2024, https://doi.org/10.22033/ESGF/CMIP6.6595.

Williams, A. P., and Coauthors, 2015a: Correlations between components of the water balance and burned area reveal new insights for predicting forest fire area in the southwest United States. *Int. J. Wildland Fire*, **24**, 14–26, https://doi.org/10.1071/WF14023.

——, R. Seager, J. T. Abatzoglou, B. I. Cook, J. E. Smerdon, and E. R. Cook, 2015b: Contribution of anthropogenic warming to California drought during 2012–2014. *Geophys. Res. Lett.*, **42**, 6819–6828, https://doi.org/10.1002/2015GL064924.

Xie, S.-P., and Y. Kosaka, 2017: What caused the global surface warming Hiatus of 1998–2013? *Curr. Climate Change Rep.*, **3**, 128–140, https://doi.org/10.1007/s40641-017-0063-0.

Yang, L., S. Chen, C. Wang, D. Wang, and X. Wang, 2018: Potential impact of the Pacific decadal oscillation and sea surface temperature in the tropical Indian ocean–western Pacific on the variability of typhoon landfall on the China Coast. *Climate Dyn.*, **51**, 2695–2705, https://doi.org/10.1007/s00382-017-4037-7.

Yang, Q., Z. Ma, X. Fan, Z.-L. Yang, Z. Xu, and P. Wu, 2017: Decadal modulation of precipitation patterns over eastern China by sea surface temperature anomalies. *J. Climate*, **30**, 7017–7033, https://doi.org/10.1175/JCLI-D-16-0793.1.

Yoon, J., and S.-W. Yeh, 2010: Influence of the Pacific decadal oscillation on the relationship between El Niño and the northeast Asian summer monsoon. *J. Climate*, **23**, 4525–4537, https://doi.org/10.1175/2010JCLI3352.1.

You, Y., and J. C. Furtado, 2017: The role of South Pacific atmospheric variability in the development of different types of ENSO. *Geophys. Res. Lett.*, **44**, 7438–7446, https://doi.org/10.1002/2017GL073475.

Zebiak, S. E., and M. A. Cane, 1987: A model El Niño–Southern Oscillation. *Mon. Wea. Rev.*, **115**, 2262–2278, https://doi.org/10.1175/1520-0493(1987)115<2262:AMENO>2.0.CO;2.

Zhang, L., and T. L. Delworth, 2015: Analysis of the characteristics and mechanisms of the Pacific decadal oscillation in a suite of coupled models from the geophysical fluid dynamics laboratory. *J. Climate*, **28**, 7678–7701, https://doi.org/10.1175/JCLI-D-14-00647.1.

Zhang, Y., S.-P. Xie, Y. Kosaka, and J.-C. Yang, 2018: Pacific decadal oscillation: Tropical Pacific forcing versus internal variability. *J. Climate*, **31**, 8265–8279, https://doi.org/10.1175/JCLI-D-18-0164.1.

Zhao, S., Y. Deng, and R. X. Black, 2017: Observed and simulated spring and summer dryness in the United States: The impact of the Pacific Sea surface temperature and beyond. *J. Geophys. Res. Atmos.*, **122**, 12 713–12 731, https://doi.org/10.1002/2017JD027279.

Zhao, Y., M. Newman, A. Capotondi, E. Di Lorenzo, and D. Sun, 2021: Removing the effects of tropical dynamics from North Pacific climate variability. *J. Climate*, **34**, 9249–9265, https://doi.org/10.1175/JCLI-D-21-0344.1.

——, E. Di Lorenzo, M. Newman, A. Capotondi, and S. Stevenson, 2023: A Pacific tropical decadal variability challenge for climate models. *Geophys. Res. Lett.*, **50**, e2023GL104037, https://doi.org/10.1029/2023GL104037.

Zhu, Y., H. Wang, J. Ma, T. Wang, and J. Sun, 2015: Contribution of the phase transition of Pacific decadal oscillation to the late 1990s' shift in East China summer rainfall. *J. Geophys. Res. Atmos.*, **120**, 8817–8827, https://doi.org/10.1002/2015JD023545.

Ziehn, T., and Coauthors, 2019: CSIRO ACCESS-ESM1.5 model output prepared for CMIP6 CMIP historical. Earth System Grid Federation, accessed 1 February 2024, https://doi.org/10.22033/ESGF/CMIP6.4272.